RESEARCH PAPER

Interfacial instability of liquid films coating the walls of a parallel-plate channel and sheared by a gas flow

Miklós Vécsei[1,2] · Mathias Dietzel[1] · Steffen Hardt[1]

Abstract

The stability and coupling of liquid films coating the walls of a parallel-plate channel and sheared by a pressure-driven gas flow along the channel center plane is studied. The films are susceptible to a long-wavelength instability. For sufficiently low Reynolds numbers and thick gas layers, the dynamic behavior is found to be described by two coupled nonlinear partial differential equations. A linear stability analysis is conducted under the condition that the material properties and the initial undisturbed liquid-film thicknesses are equal. The linear analysis is utilized to determine whether the interfaces are predominantly destabilized by the variations of the shear stress or by the pressure gradient acting upon them. The analysis of the weakly nonlinear equations performed for this case shows that instabilities corresponding to a vanishing Reynolds number are absent from the system. Moreover, for this configuration, the patterns emerging along the two interfaces are found to be identical in the long-time limit, implying that the films are fully synchronized. A different setup, where the liquid films have identical material properties but their undisturbed thicknesses differ, is studied numerically. The results show that, even for this configuration, the interfacial waves remain phase-synchronized and closely correlated for an extended period of time. These findings are particularly relevant for gaseous flow through narrow ducts with liquid-coated walls.

1 Introduction

Multiphase flows through ducts and pipes are widespread in engineering applications such as power plants and crude oil transport. Depending on the volume fraction of the gaseous phase, one distinguishes bubbly, slug, churn, and annular flows (Weisman 1983; Brennen 2005). In recent years, there has been a strong interest in using structured or porous surfaces soaked with a liquid to create surfaces being robustly

✉ Steffen Hardt
hardt@nmf.tu-darmstadt.de

Miklós Vécsei
vecsei.miklos@wigner.mta.hu

Mathias Dietzel
dietzel@nmf.tu-darmstadt.de

1   Institute for Nano- and Microfluidics, TU Darmstadt, Alarich-Weiss-Str. 10, 64287 Darmstadt, Germany

2   Department of Plasma Physics, Wigner Research Centre for Physics, Konkoly-Thege Miklós Road 29-33, Budapest 1121, Hungary

repellent to another fluid (Wong et al. 2011; Grinthal and Aizenberg 2013). In that context, a simple process has been demonstrated to impregnate planar walls with a stable, non-dewetting water-repelling film (Eifert et al. 2014). When functionalizing microchannel walls based on these methods, flow patterns similar to annular flows prevail, where a fluid is pumped through channels whose walls are coated with a thin liquid film. Such flows may give rise to instabilities, which are, in fact, quite common in nature. One of the most well-known related phenomena is the Kelvin–Helmholtz instability, appearing on the initially flat interface between two inviscid fluid layers flowing parallel to each other. If the velocity of the two fluids differs, the system may be unstable to small disturbances in the flow field (Drazin and Reid 2004). The disturbances are escalated by the corresponding variations in the dynamic (Bernoulli) pressure and grow into a vortex sheet (Chandrasekhar 2013). If the viscous stresses are not negligibly small, they may also trigger the formation of patterns at interfaces. An example is the formation of ripples on sand beds sheared by a liquid flow (Charru and Hinch 2006). Therefore, for general co-current fluid flows, it is reasonable to consider the variations in both the pressure and the viscous stresses to obtain the time evolution of the system. Since the early discussion of Yih (1967), the instability of

the parallel flow of fluids with different viscosities has been the subject of numerous papers. For instance, as a far from exhaustive selection, the reader is referred to Gondret and Rabaud (1997), Joseph et al. (1984), and Hooper and Boyd (1983), as well as to Yiantsios and Higgins (1988). The shear number of other studies referencing this selection of papers illustrates the importance and considerable challenge the analysis of co-current viscous flow often poses.

This paper investigates the coupled hydrodynamic instabilities of two thin liquid films coating flat walls opposite to each other when exposed to gas flow. Apart from the already mentioned example of liquid-infused surfaces, the corresponding flow patterns are important for a number of applications such as microchannel cooling (Kandlikar 2012; Houshmand and Peles 2013; Kabov et al. 2011). In addition, the understanding of interfacial instabilities in gas–liquid flows is vital for the mapping of the different flow regimes in confined multiphase systems. These maps have been explored analytically (Taitel and Dukler 1976), experimentally (Saisorn and Wongwises 2008; Triplett et al. 1999), and numerically (Talimi et al. 2012). Although core-annular flows have, in general, different properties than planar flows, their features are similar as long as the tube curvature and the corresponding capillary effects are negligibly small (Renardy 1987). Core-annular gas flow can be utilized as a model system for the discussion of the closure of airways (Heil et al. 2008; Johnson et al. 1991; Halpern et al. 2008). A review of various instabilities of core-annular flows was given by Joseph et al. (1997).

For thin liquid films, interfacial instabilities are strongly influenced by surface tension. The stabilizing effect of capillarity dampens sharp deformations of the interface, so that, for sufficiently thin films, the evolution of the instabilities can be described by the long-wavelength approximation. The analyses of these systems have shown that the co-current flow of two superposed liquid films with large interfacial tension is governed by the Kuramoto–Sivashinsky equation (Hooper and Grimshaw 1985; Shlang et al. 1985). The analysis of this nonlinear partial differential equation is remarkably challenging. Interfacial instabilities occurring in the planar flow of three superposed liquid films have been first discussed by Li (1969). Although the systems may be studied by linear stability analysis (Kliakhandler and Sivashinsky 1995), the large influence of the nonlinear terms severely limits the range of validity of the linearized problem. It has been argued that the weakly nonlinear equations of stratified films should take the form of coupled Kuramoto–Sivashinsky equations (Papaefthymiou et al. 2013; Papaefthymiou and Papageorgiou 2017). The analysis of the equations revealed that in contrast to double-layer configurations, these systems can become unstable even if inertial effects are negligibly small. These novel instabilities were found to be either the result of a resonance-like coupling between the interfaces or were assumed to be a fourth-order

generalization of the Majda–Pego instability (Majda and Pego 1985; Papaefthymiou et al. 2013).

The mathematical complexity of multilayer systems hinders their analytical description. This restricts the investigations to either numerical simulations or to the discussion of simplified configurations (Renardy 1987; Kliakhandler and Sivashinsky 1995; Papaefthymiou et al. 2013; Papaefthymiou and Papageorgiou 2017). For the long-wavelength instability driven by a planar gas flow between thin liquid films, the disparity between the viscosities of the liquid and the gas phase allows for a simplification of the governing equations. This is the focus of this paper. Section 2 discusses the derivation of the evolution equations for the film thicknesses. Section 3 addresses symmetric systems, where the compact form of the equations and the small number of independent parameters permits a deeper analytical treatment. Finally, in Sect. 4, a brief summary is given of the results obtained by numerically simulating asymmetric systems. Based on linear stability analysis, a qualitative explanation for the observed behavior is given.

2 Evolution equations of the interfaces

2.1 Governing equations

In this section, the evolution equations for the gas and liquid-film flows are derived. The analysis in two spatial dimensions is restricted to immiscible, incompressible, Newtonian fluids. The latter two assumptions imply sufficiently small flow velocities and shear rates, respectively. Furthermore, the flow is assumed to be driven solely by an externally imposed pressure gradient. According to the notations introduced in Fig. 1, the momentum equations in the bulk fluids and the stress balance at the interfaces are given by the following:

$$\rho_i \frac{d\boldsymbol{v}}{dt} = \boldsymbol{\nabla} \cdot \mathbf{T}_i, \tag{1}$$

$$0 = (-1)^i \gamma_i \left(\boldsymbol{\nabla}_i \cdot \hat{\mathbf{n}}_i \right) \hat{\mathbf{n}}_i + \left(\mathbf{T}_g - \mathbf{T}_i \right) \hat{\mathbf{n}}_i, \tag{2}$$

where the liquid films are assumed to be sufficiently thin to neglect the gravitational force. The subscript i defines the
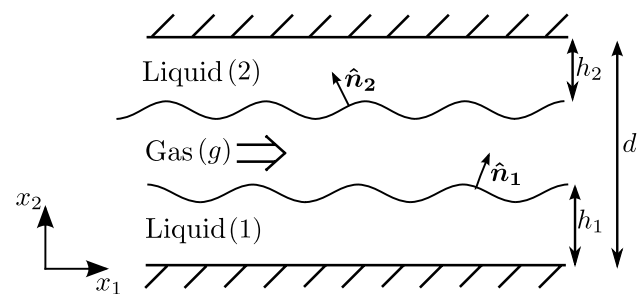

Fig. 1 Illustration of gas flow between two liquid films

fluid film or the interface the physical quantity is referring to. In this sense and as illustrated in Fig. 1, in Eq. (1), the three phases are referred to as "1", "g", and "2" from bottom to top. In a similar manner, in Eq. (2), the lower interface is denoted by "1" and the upper one by "2". The gradient along interface i is denoted by ∇_i, and its normal vector by $\hat{\mathbf{n}}_i$. The directions of $\hat{\mathbf{n}}_i$ are defined in Fig. 1. The symbols ρ_i and γ_i refer to the mass densities of the fluids and the constant surface tensions, respectively. The velocity field is denoted by $\mathbf{v} = (v_1, v_2)$, and its material (or substantial) time derivative by $d\mathbf{v}/dt \equiv \partial\mathbf{v}/\partial t + \mathbf{v} \cdot \nabla\mathbf{v}$. The stress tensors, $\mathbf{T}_i$, are composed of the scalar hydrodynamic pressures p_i and the viscous stress tensors: $\mathbf{E}_i$.

$$
\begin{aligned}
\mathbf{T}_i &= -p_i \mathbf{I} + \mathbf{E}_i, \\
[\mathbf{E}_i]_{kl} &= \mu_i \left(\frac{\partial v_k}{\partial x_l} + \frac{\partial v_l}{\partial x_k} \right) \qquad k,l \in [1,2],
\end{aligned}
\tag{3}
$$

where the identity matrix is referred to by $\mathbf{I}$, while μ_i denote the dynamic viscosities. This study is limited to instabilities with characteristic time scales much smaller than the gravitational time scale, i.e., for films with a small Bond number. Most prominently and as assumed in this work, this condition is met for sufficiently thin films, so that the effects of interfacial stresses markedly exceed those of the volumetric forces.

For the nondimensionalization of the equations, one introduces λ_{char} as a characteristic length scale of the variation of the flow field along the horizontal direction. An educated guess for this quantity is the still unknown linear approximation of the characteristic wavelength of the instability. It is emphasized that a different choice for this scaling length does not affect the underlying physics of the problem. One simply has to ensure posteriori that no horizontal characteristic length scale found in the course of the analysis is significantly smaller than the chosen one. Consequently, the x_1 coordinate is nondimensionalized by $X = x_1/\lambda_{\text{char}}$. With d denoting the separation distance between the walls, the quantities $Y = x_2/d$ and $H_i = h_i/d$ are introduced as the dimensionless vertical coordinate and film thickness, respectively. The volume flux of the gas flow at the entrance of the channel, Q, is utilized for defining the dimensionless velocities $V = (V_X, V_Y) = (v_1, v_2/\epsilon)d/Q$. In this definition, the $\epsilon = d/\lambda_{\text{char}}$ parameter appearing in the vertical velocity originates from the different spatial scalings applied in the horizontal and the vertical directions. The rescaled time variable reads $\tau = tQ/(\lambda_{\text{char}}d)$. The dimensionless pressures are given by $P_i = p_i \epsilon d^2/(\mu_g Q)$, with μ_g being the dynamic viscosity of the gaseous medium. Finally, the viscosity ratios $M_i = \mu_i/\mu_g$ and density ratios $R_i = \rho_i/\rho_g$ are introduced. With these new variables, the momentum equations take the form

$$
\begin{aligned}
\epsilon Re\, R_i \frac{dV_X}{d\tau} &= M_i \left(\epsilon^2 \frac{\partial^2 V_X}{\partial X^2} + \frac{\partial^2 V_X}{\partial Y^2} \right) - \frac{\partial P_i}{\partial X}, \\
\epsilon^3 Re\, R_i \frac{dV_Y}{d\tau} &= M_i \left(\epsilon^4 \frac{\partial^2 V_Y}{\partial X^2} + \epsilon^2 \frac{\partial^2 V_Y}{\partial Y^2} \right) - \frac{\partial P_i}{\partial Y}.
\end{aligned}
\tag{4}
$$

The Reynolds number is denoted by $Re = \rho_g Q/\mu_g$. The interfacial stress balance in the tangential and the normal directions is given by the following:

$$
\begin{aligned}
&\left(\epsilon^2 \frac{\partial V_Y}{\partial X}\bigg|_g + \frac{\partial V_X}{\partial Y}\bigg|_g \right) - M_i \left(\epsilon^2 \frac{\partial V_Y}{\partial X}\bigg|_i + \frac{\partial V_X}{\partial Y}\bigg|_i \right) \\
&\quad = -\frac{4\epsilon^2 \partial H_i/\partial X}{1 - \epsilon^2(\partial H_i/\partial X)^2} \left(\frac{\partial V_Y}{\partial Y}\bigg|_g - M_i \frac{\partial V_Y}{\partial Y}\bigg|_i \right), \\
&P_i - P_g + 2\epsilon^2 \frac{1 + \epsilon^2(\partial H_i/\partial X)^2}{1 - \epsilon^2(\partial H_i/\partial X)^2} \left(\frac{\partial V_Y}{\partial Y}\bigg|_g - M_i \frac{\partial V_Y}{\partial Y}\bigg|_i \right) \\
&\quad = (-1)^i \frac{\epsilon}{Ca_i} \frac{\partial^2 H_i/\partial X^2}{[\epsilon^2(\partial H_i/\partial X)^2 + 1]^{3/2}} \quad i \in [1,2].
\end{aligned}
$$

The capillary numbers are denoted by $Ca_i = \mu_g Q/(\epsilon^2 d\gamma_i)$. This definition ensures that the capillary number is of $O(1)$.

Finally, the dimensionless continuity equation in the layers read

$$
\frac{\partial V_X}{\partial X} + \frac{\partial V_Y}{\partial Y} = 0,
\tag{5}
$$

while the kinematic condition along the interfaces leads to

$$
\begin{aligned}
&\frac{\partial H_1}{\partial \tau} + V_X\bigg|_{H_1} \frac{\partial H_1}{\partial X} - V_Y\bigg|_{H_1} = 0, \\
&\frac{\partial H_2}{\partial \tau} + V_X\bigg|_{1-H_2} \frac{\partial H_2}{\partial X} + V_Y\bigg|_{1-H_2} = 0.
\end{aligned}
\tag{6}
$$

2.2 Framework of the analysis

The current paper focuses on systems where the material properties of the liquids are identical. Formally, this implies that $M_1 = M_2 \equiv M$, $Ca_1 = Ca_2 \equiv Ca$ and $R_1 = R_2 \equiv R$. To ease the mathematical analysis, the following simplifications are introduced.

Assumption 1 The dominant influence of capillarity and viscosity on the behavior of thin liquid films dampens short-wavelength deformations and instabilities along their interfaces. Therefore, the long-wavelength approximation (Oron et al. 1997) is utilized.

Assumption 2 In contrast to related work (Papaefthymiou and Papageorgiou 2017), inertial effects in the gas flow are included. However, to limit the scope of the present

analysis, the Reynolds number for the gas will be restricted to configurations where $O(\epsilon Re) < 1$. Consequently, terms of $O(\epsilon Re)^2$ and higher are negligible. Nevertheless, given the high viscosity ratio between the liquid and the gaseous medium, the Reynolds number and the corresponding nonlinear terms in the momentum equation of the liquid layers are negligible.

Assumption 3   To reduce the set of equations to only two evolution equations, it is sufficient to apply the previous two assumptions. However, these equations are highly complex, and related studies usually focus on either the numerical analysis of these systems for a restricted parameter space (Papaefthymiou et al. 2013) or utilize strong simplifications, such as negligible surface tension and inertia (Papaefthymiou and Papageorgiou 2017). To facilitate analytical studies and to retain some of the physical insight of the problem, the current work is based in the assumption that the viscosity of the gas is much smaller than that of the liquid so that $M^2 \gg 1$. In the following, this assumption is referred to as the assumption of semi-rigidness of the liquid films. Consequently, all terms containing second or higher orders of $1/M$ are neglected from the equations of the current study. As detailed in Appendix 1, this assumption yields a good approximation for the time evolution of the system as long as $O(1/M) \leq O(\epsilon)$.

The mathematical implementation of these assumptions is straightforward and is summarized in Appendix 1. It is found that, to leading order of ϵ and $1/M$, the system is characterized by the equations:

$$\frac{\partial H_1}{\partial \overline{\tau}} = -\frac{\partial}{\partial \overline{X}} \left\{ \frac{H_1^2(3 + H_1 - 3H_2)}{\epsilon(1 - H_1 - H_2)^3} + \frac{H_1^3}{3}\frac{\partial^3 H_1}{\partial \overline{X}^3} \right.$$
$$\left. + Re\sqrt[3]{Ca}\frac{3H_1^2(1 + 5H_1 - H_2)}{35(1 - H_1 - H_2)^3}\left(\frac{\partial H_1}{\partial \overline{X}} + \frac{\partial H_2}{\partial \overline{X}} \right) \right\},$$
(7)

$$\frac{\partial H_2}{\partial \overline{\tau}} = -\frac{\partial}{\partial \overline{X}} \left\{ \frac{H_2^2(3 + H_2 - 3H_1)}{\epsilon(1 - H_1 - H_2)^3} + \frac{H_2^3}{3}\frac{\partial^3 H_2}{\partial \overline{X}^3} \right.$$
$$\left. + Re\sqrt[3]{Ca}\frac{3H_2^2(1 + 5H_2 - H_1)}{35(1 - H_1 - H_2)^3}\left(\frac{\partial H_1}{\partial \overline{X}} + \frac{\partial H_2}{\partial \overline{X}} \right) \right\}.$$
(8)

To obtain these equations, the temporal and spatial coordinates have been rescaled as $\overline{\tau} = \tau\epsilon\sqrt[3]{Ca/M}$ and $\overline{X} = \sqrt[3]{Ca}X$. In the following, to avoid complicated notations, the overbars will be omitted.

It is noted that, in the previous studies, it has already been implied that the evolution equations for the liquid-film thicknesses take a form similar to Eqs. (7) and (8), even for arbitrary viscosity ratios (Papaefthymiou et al. 2013). In the general case, these equations are remarkably complex, and, to the best of our knowledge, the full evolution equations have not been presented in the literature so far, neither for arbitrary $1/M$ nor for $1/M < 1$.

In contrast to other applications of the lubrication approximation to study the dynamics of thin films, Eqs. (7) and (8) explicitly depend on the scaling parameter ϵ. First, given the underlying expansion of the governing equations in ϵ, the final evolution equations will, in general, always contain terms of mixed order in ϵ. Most prominently, the capillary term is of cubic order in ϵ, but this is commonly hidden in the use of the scaled capillary number. While, in the absence of a gas flow, the stress terms in the film evolution equation are typically of linear and cubic order in ϵ, for systems with a gas flow this is supplemented by a stress term of zeroth order. This represents the stress from the base gas flow onto the liquids and as such has no characteristic length scale in the spread direction of the films. In essence, the evolution of the interfaces depends on the stresses of both the base flow and the additional perturbative effects caused by the inertia of the gaseous medium and the capillary pressure. The significance of the latter two effects relative to that of the base flow is expressed by ϵ. This parameter simply scales the nondimensional stress terms in a fashion, such that naturally evolving spatial periodicity is properly scaled to the chosen lateral length scale of the (nondimensional) domain. In a dimensionful notation, ϵ would not be present.

Nevertheless, although Eqs. (7) and (8) seem to imply that there is a singularity in the equations for $\epsilon \to 0$, it can be verified that it only appears due to the introduction of $\overline{X}$ and $\overline{\tau}$ to Eqs. (7) and (8). Even in the limit $\epsilon \to 0$, a nonsingular evolution of the system is obtained for the original temporal and spatial variables.

2.3 Physical interpretation of the problem

In Fig. 2, to provide an intuitive understanding of the physical background for Eqs. (7) and (8), an example of the flow field of the gaseous medium for $Re = 2$ and $\epsilon = 0.1$ in a symmetrically deformed channel is shown. Within the framework of the current study, liquid interfaces deformed in the same way as the channel walls of Fig. 2 would generate identical flow profiles in the gas. The *Mathematica*® software package is used to evaluate the obtained analytic formulas with the
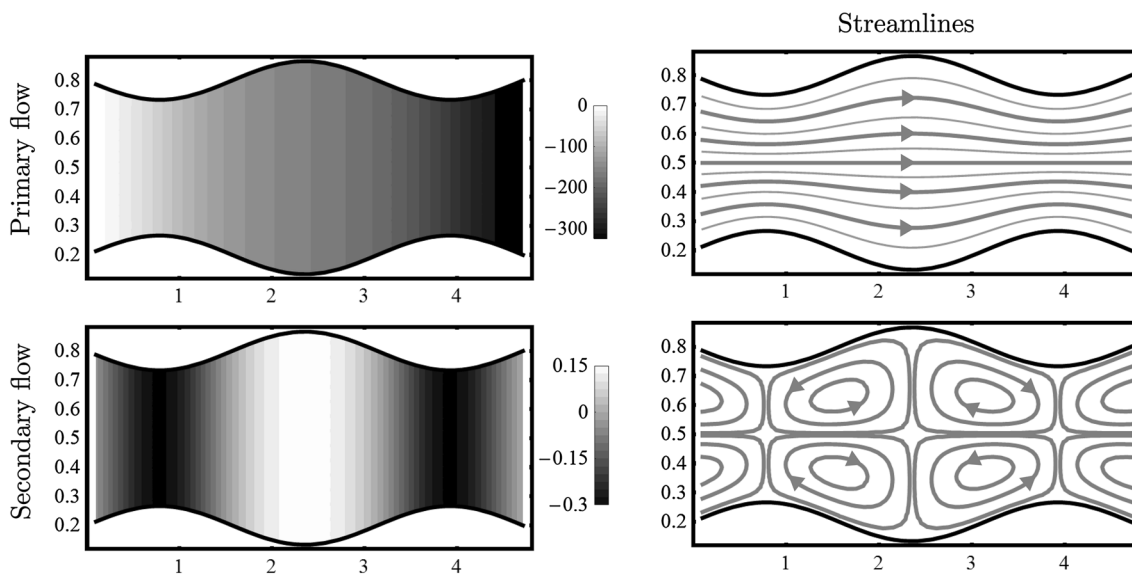
Fig. 2 Pressure drop and streamlines of an exemplary gas flow in a channel with symmetrically deformed walls. The Stokes flow (primary flow) is depicted in the first row, while the first-order correction arising from the nonzero inertial terms is shown in the second one. The full flow field corresponds to the superposition of the two results ($Re = 2$, $\epsilon = 0.1$)

given nondimensional numbers. In the first row of Fig. 2, the pressure drop and the streamlines of the zeroth-order (Stokes) flow are shown, while the inertial first-order perturbation is depicted in the second row. The full (non-Stokesian) flow field can be obtained by superimposing the two results. The figure indicates that the base flow simply corresponds to a channel flow with periodically undulated walls. The first-order flow supports two instability mechanisms. First, the pressure in the narrower section is lower which will promote reducing the cross section even further. The corresponding pressure gradient is given by the following:

$$\left.\frac{\partial P_g}{\partial X}\right|_{H_1} = \left.\frac{\partial P_g}{\partial X}\right|_{1-H_2} = -\frac{6\left[70 + 9\epsilon Re\left(\frac{\partial H_1}{\partial X} + \frac{\partial H_2}{\partial X}\right)\right]}{35\left(1 - H_1 - H_2\right)^3}. \quad (9)$$

Second, the periodic lateral pressure fluctuations cause counter-rotating vortices, which deform the film interfaces by viscous stresses. These are given by

$$E|_{H_1} = -E|_{1-H_2} = \frac{6\left[35 + \epsilon Re\left(\frac{\partial H_1}{\partial X} + \frac{\partial H_2}{\partial X}\right)\right]}{35\left(1 - H_1 - H_2\right)^2}. \quad (10)$$

In a later section and based on this illustration, the significance of the normal stresses to induce the instability will be compared to that of the shear stresses.

Furthermore, one may ask how the film deformation affects the pressure gradient to maintain a constant volumetric flow rate. Based on Eq. (9), one can calculate the pressure drop along the channel of length L. Assuming that the deformations at its ends are negligibly small yields

$$P_g(L) - P_g(0) = -\int_0^L \frac{12}{(1 - H_1 - H_2)^3}\, dX. \quad (11)$$

The effect of the gas dragging the liquid films is not considered in the expression, since the corresponding term contributes to the evolution equations only at higher orders of the viscosity ratios. This is beyond the scope of the current analysis. Assuming the system to be mirror-symmetric, the notation $H_1 = H_2 = H_0 + \Delta H$ is introduced. Here, H_0 represents the initial uniform film thickness and the local deviation from that state is given by ΔH. The integral takes the form

$$P_g(L) - P_g(0) = -\int_0^L \left[\frac{12}{(1 - 2H_0)^3} + \frac{72\Delta H}{(1 - 2H_0)^4}\right. \quad (12)$$
$$\left. + \frac{288\Delta H^2}{(1 - 2H_0)^5} + \frac{960\Delta H^3}{(1 - 2H_0)^6} + \cdots\right] dX.$$

The linear term in ΔH drops out, since the total volume of the liquid films does not change during their evolution. Thus, since, in relevant scenarios, $|\Delta H/(1 - 2H_0)| \ll 1$, the term scaling with ΔH^2 defines the dominant effect of the deformations of the liquid surfaces. In comparison to the case of undeformed films, this term implies the pressure drop to be $1 + O(\Delta H)^2 \times 24/(1 - 2H_0)^2$ times larger due to the instability of the interfaces.

3 Symmetric systems

This section discusses systems where the undisturbed liquid-film thicknesses are equal, i.e., the undisturbed system is completely symmetric with respect to the channel center plane. The question arises whether or not the mirror symmetry breaks down during the evolution of the system. As a similar problem, the breakdown of axial symmetry in core-annular flows has been observed in experiments (Hewitt and Hall-Taylor 1970) and in analytical studies (Renardy 1987), supporting the significance of this question for planar flows.

With the initial film thickness H_0, we denote the film deformations as $\Delta H_1 = H_1 - H_0$ and $\Delta H_2 = H_2 - H_0$. In the case of small deformations $\Delta H_1 \equiv \epsilon \eta_1$, $\Delta H_2 \equiv \epsilon \eta_2$ are introduced, where $O(\eta_1) = O(\eta_2) = O(1)$, while $0 < \epsilon < 1$. Then, one finds that, after neglecting second or higher orders of ϵ, Eqs. (7) and (8) transform to

$$
\begin{aligned}
\frac{\partial \eta_1}{\partial \tau} = -\frac{\partial}{\partial X} \Bigg\{ & \frac{6H_0[(1-H_0)\eta_1 + H_0\eta_2]}{\epsilon(1-2H_0)^4} \\
& + Re\sqrt[3]{Ca}\frac{3H_0^2(1+4H_0)}{35(1-2H_0)^3}\left(\frac{\partial \eta_1}{\partial X} + \frac{\partial \eta_2}{\partial X}\right) \\
& + \frac{3[(1-H_0)\eta_1 + H_0\eta_2]}{(1-2H_0)^5}[(1+H_0(3-2H_0))\eta_1 \\
& + H_0(3+2H_0)\eta_2] + \frac{H_0^3}{3}\frac{\partial^3 \eta_1}{\partial X^3} \Bigg\},
\end{aligned}
\tag{13}
$$

$$
\begin{aligned}
\frac{\partial \eta_2}{\partial \tau} = -\frac{\partial}{\partial X} \Bigg\{ & \frac{6H_0[(1-H_0)\eta_2 + H_0\eta_1]}{\epsilon(1-2H_0)^4} \\
& + Re\sqrt[3]{Ca}\frac{3H_0^2(1+4H_0)}{35(1-2H_0)^3}\left(\frac{\partial \eta_1}{\partial X} + \frac{\partial \eta_2}{\partial X}\right) \\
& + \frac{3[(1-H_0)\eta_2 + H_0\eta_1]}{(1-2H_0)^5}[(1+H_0(3-2H_0))\eta_2 \\
& + H_0(3+2H_0)\eta_1] + \frac{H_0^3}{3}\frac{\partial^3 \eta_2}{\partial X^3} \Bigg\}.
\end{aligned}
\tag{14}
$$

The first and the second terms in the curly brackets represent the stresses acting from the primary flow of the gas on the film. The governing equations remain nonlinear in η_1 and η_2. In general, such a nonlinearity can not be scaled out by a Galilean transformation (Papaefthymiou et al. 2013). This restricts the validity of the linear stability analysis of the equations to a very narrow region around the equilibrium state.

3.1 Linear stability analysis

The remaining nonlinear terms of Eqs. (13) and (14) imply that their linearization in η_1 and η_2 is only expected to reliably

approximate the evolution of the interfaces for extremely small deformations. However, the analysis is helpful for a subsequent discussion of the weakly nonlinear equations. Furthermore, the linear analysis also gives approximate values for the scaling parameters of the system.

Assuming that, instead of $O(\eta_1) = O(\eta_2) = O(1)$ proposed for Eqs. (13) and (14), $\eta_1, \eta_2 \ll \epsilon < 1$, one can neglect the second-order terms in the deformations from Eqs. (13) and (14). The resulting system of linear partial differential equations can be analyzed utilizing Fourier transformation (Cross and Greenside 2009). One finds the solution of the equations to be given by

$$
\begin{pmatrix} \eta_1 \\ \eta_2 \end{pmatrix} = \int_{-\infty}^{\infty} \left(A_+ \mathbf{v}_+ e^{\sigma_+ \tau} + A_- \mathbf{v}_- e^{\sigma_- \tau} \right) e^{ikX} dk, \quad \text{where}
$$

$$
\mathbf{v}_+ = \begin{pmatrix} 1 \\ 1 \end{pmatrix}, \quad \sigma_+ = -ik\frac{6H_0}{\epsilon(1-2H_0)^4} - k^4\frac{H_0^3}{3}
$$
$$
+ k^2 Re\sqrt[3]{Ca}\frac{6}{35}\frac{H_0^2(1+4H_0)}{(1-2H_0)^3},
$$

$$
\mathbf{v}_- = \begin{pmatrix} 1 \\ -1 \end{pmatrix}, \quad \sigma_- = -ik\frac{6H_0}{\epsilon(1-2H_0)^3} - k^4\frac{H_0^3}{3},
$$

$$
\tag{15}
$$

with k being the dimensionless wave number and $A_\pm(k)$ being the Fourier amplitudes. From this, it is apparent that the deformations of the interfaces are the superposition of a symmetric instability, $\mathbf{v}_+$, and a linearly independent antisymmetric one, $\mathbf{v}_-$. As $\text{Im}(\sigma_\pm) \propto k$, the propagation speeds of the linear interfacial waves are independent of the wavenumber and, therefore, do not disperse. Furthermore, $\text{Re}(\sigma_-) < 0$ for all wavenumbers, while $\text{Re}(\sigma_+) > 0$ for sufficiently small wavenumbers. Consequently, the interfaces are always linearly unstable for the symmetric deformations, while the antisymmetric ones are linearly stable.

On one hand, the characteristic (i.e., dominant) wavenumber of the deformations can be assumed to correspond to the wavenumber maximizing σ_+ (i.e., the fastest growing wavenumber), which is given by

$$
k_{\text{char}} = \left[\frac{9}{35} Re\sqrt[3]{Ca}\frac{1+4H_0}{H_0(1-2H_0)^3} \right]^{1/2}.
\tag{16}
$$

Hence, owing to the negligible effect of gravity, the films are always inherently unstable to disturbances of a sufficiently small wavenumber for nonvanishing Re.

On the other hand, according to Sect. 2.2, the dimensionless X coordinate is given by $X = x_1 \sqrt[3]{Ca}/\lambda_{\text{char}}$, where λ_{char} is the linear approximation of the characteristic dimensional wavelength of the deformations. Thus, consistent scaling requires that $k_{\text{char}} = 2\pi/\sqrt[3]{Ca}$. The equivalence of this

wavenumber to the one from Eq. (16) provides an expression for Ca given by

$$Ca = \frac{140\pi^2 H_0 (1 - 2H_0)^3}{9Re(1 + 4H_0)}. \qquad (17)$$

With the definition of the capillary number, one may also compute ϵ to be given by

$$\epsilon = \sqrt{\frac{9\mu_g QRe(1 + 4H_0)}{140\pi^2 d\gamma H_0 (1 - 2H_0)^3}} = \sqrt{\frac{9\rho_g Q^2 (1 + 4H_0)}{140\pi^2 d\gamma H_0 (1 - 2H_0)^3}}. \qquad (18)$$

As shown in Eq. (18), if ϵ is defined consistently, it is merely a parameter predetermined by the properties of the system. The neutrally stable wavenumber is obtained from the condition $\mathrm{Re}(\sigma_+) = 0$. According to Eq. (15), this condition is satisfied at $k_{\max} = \sqrt{2}k_{\mathrm{char}}$.

To illustrate the application range of the current study, typical values of the dimensionless numbers used in the examples presented in the following sections are summarized in Table 1.

3.1.1 Physical interpretation of the results

First, one may utilize the results of the linear stability analysis to judge the relative influence of the pressure gradient and the viscous stresses, respectively, on the instability. For this purpose, one assumes that both effects may be considered separately from one another. Without the presence of viscous stresses along the interface, the system would still be unstable, but with the characteristic wavenumber $k_{\mathrm{char}}^{\mathrm{P}}$. This instability emerges due to a mechanism analogous to the Venturi effect. Namely, it is caused by the fluctuation in the dynamic pressure of the gas flow triggered by the widening or narrowing of the gas layer with changing liquid-layer thicknesses. An equivalent mechanism is responsible for the Kelvin–Helmholtz instability. This is depicted in the bottom-left graph of Fig. 2. Similarly, if the pressure gradient is omitted from the evolution equations, one obtains $k_{\mathrm{char}}^{\mathrm{T}}$ for the characteristic wavenumber. The instability driven by the viscous stresses is triggered by the "sweeping" mechanism of the counter-rotating vortices of the secondary air flow before and after an elevation of the liquid–gas interface. This is shown in the bottom-right graph of Fig. 2. A straightforward calculation leads to

$$k_{\mathrm{char}}^{\mathrm{P}} = \left[\frac{54}{35} Re \sqrt[3]{Ca} \frac{1}{(1 - 2H_0)^3} \right]^{1/2}, \qquad (19)$$

$$k_{\mathrm{char}}^{\mathrm{T}} = \left[\frac{9}{35} Re \sqrt[3]{Ca} \frac{1}{(1 - 2H_0)^2 H_0} \right]^{1/2}. \qquad (20)$$

Table 1 Dimensionless quantities, their definitions, and typical values of the dimensionless numbers employed in the numerical simulations of the study

Notation	Definition	Range
X	$x_1/\lambda_{\mathrm{char}}$	–
Y	x_2/d	–
τ	$tQ/(\lambda_{\mathrm{char}}d)$	–
H_i	h_i/d	–
V_X	$v_1 d/Q$	–
V_Y	$v_2 \epsilon d/Q$	–
P_i	$p_i \epsilon d^2/(\mu_g Q)$	–
H_0	$(H_1 + H_2)/2\big|_{t=0}$	0.04–0.2
δ	$(H_1 - H_2)\big|_{t=0}$	0–2
ϵ	$d/\lambda_{\mathrm{char}}$	0.02–0.16
M_i	μ_i/μ_g	48–500
R_i	ρ_i/ρ_g	859–863
Re	$\rho_g Q/\mu_g$	10–33
Ca_i	$\mu_g Q/(\epsilon^2 d\gamma_i)$	0.1–0.56

The obtained wavenumbers can be related to the original one given by Eq. (16) with the expression $k_{\mathrm{char}}^2 = (k_{\mathrm{char}}^{\mathrm{P}})^2 + (k_{\mathrm{char}}^{\mathrm{T}})^2$. Moreover, as long as $H_0 < 0.125$ ($H_0 > 0.125$), $k_{\mathrm{char}}^{\mathrm{T}} > k_{\mathrm{char}}^{\mathrm{P}}$ ($k_{\mathrm{char}}^{\mathrm{T}} < k_{\mathrm{char}}^{\mathrm{P}}$). This suggests that, at small film thicknesses, the interfaces are mainly deformed by viscous stresses, while, for larger film thicknesses, the instabilities are driven by pressure gradients.

Second, one may be interested in the effect which the coupling between the two interfaces has on the emergence of the patterns. That is, one can analyze how the properties of the instability of the two coupled interfaces differ from those of the instability that would appear if the deformation of one layer would not affect the other interface (Vécsei et al. 2014). The mathematical implementation of the latter scenario corresponds to setting $\eta_2 = 0$ in Eq. (13) and $\eta_1 = 0$ in Eq. (14). Performing a linear stability analysis indicates that the characteristic wavenumber of such a configuration is given by

$$k_{\mathrm{char}}' = \left[\frac{9}{70} Re \sqrt[3]{Ca} \frac{1 + 4H_0}{H_0 (1 - 2H_0)^3} \right]^{1/2}. \qquad (21)$$

Hence, the characteristic wavenumber is $\sqrt{2}$ times smaller than for the coupled system. Furthermore, its corresponding growth rate is one-fourth of the growth rate of the coupled system at $k = k_{\mathrm{char}}$. Hence, the coupling between the interfaces further destabilizes the system.

3.1.2 Validity range of the assumptions

With respect to assumption 1 Regarding the requirement that $\epsilon^2 \ll 1$, the permittable volumetric fluxes as a function of H_0 and the material properties are readily given by Eq. (18).

With respect to assumption 2 With respect to ϵRe, the corresponding first-order perturbation approach is readily justified for small ϵRe. Nevertheless, one expects the calculation to be sufficiently accurate as long as the advection-related corrections to the pressure gradient and the shear stresses in the gas layer, expressed by those terms in Eqs. (9) and (10) multiplied by ϵRe, remain small. The results of the linear stability analysis can be used to demonstrate that Eqs. (7) and (8) remain valid also at larger values of ϵRe. To show this, one assumes that $O(\partial H_1/\partial X) \approx O(\partial H_2/\partial X) \approx \Delta H k_{\mathrm{char}}$. According to Eqs. (9) and (10), if these corrections are small, then the perturbation approach for the inertial flow is justified even for larger values of ϵRe. For an antisymmetric deformation, the correction vanishes completely, while, for a symmetric deformation, the relative contribution of inertia to the pressure gradient is given by

$$\Delta P' \approx \frac{9}{35} \epsilon Re k_{\mathrm{char}} \Delta H. \tag{22}$$

An equivalent estimate for the relative contribution of inertia to the shear stresses along the interfaces is given by $\Delta E' = \Delta P'/4.5$. Thus, as long as $(\Delta P')^2 \ll 1$, the perturbation approach remains valid also at larger values of ϵRe.

With respect to assumption 3 Estimating the error introduced by neglecting terms of higher order than $1/M$ from the evolution equations requires a more careful approach, as M is absent from Eqs. (7) and (8). Although the linear behavior of multilayer systems of arbitrary viscosities has been discussed in previous studies (Anturkar et al. 1990; Renardy 1987), these were not limited to interfaces undergoing long-wavelength instabilities. Therefore, the equations arising from these calculations are more complicated and could only be solved by numerical simulations. Thus, to perform a detailed analytical description for arbitrary viscosities but within the framework of the long-wavelength approximation, it is necessary to re-derive the linearized equations, starting from Eqs. (4)–(6). For asymmetric systems, the calculations are overly complicated, but, for symmetric systems, the solution of the linearized problem can be separated into a symmetric and an independent antisymmetric instability mode. This is possible even if the intermediate layer has an arbitrary viscosity. Formally, the linear solution takes the same form as Eq. (15), where the eigenvectors remain unchanged and the difference only arises in the expression for the eigenvalues. Given the linear independency of the eigenvectors, one may calculate the growth rates for the symmetric and the antisymmetric modes separately. To this end, one first assumes that the small interfacial deformation of the interfaces is symmetric, which corresponds to eigenvector v_+. This leads to a single evolution equation for the deformations $\eta_1 = \eta_2$. Examining its Fourier transform will give the value of $\mathrm{Re}(\sigma_+)$. Similarly, one obtains $\mathrm{Re}(\sigma_-)$ by solving the linearized problem while assuming an antisymmetric deformation of the interfaces. The calculations are straightforward and were performed with the *Mathematica*® software. A comparison of the formulas obtained with this method and the numerical results of Renardy (1987) is presented in Fig. 3. The graphs show a good agreement between the two approaches. The complete expressions for the growth rates at arbitrary viscosity ratios and a more detailed discussion of the governing parameters of Fig. 3 are given in Appendix 2.

With these results, it is useful to calculate the relative error between the exact (linear) growth rates for arbitrary viscosities and those obtained for the simplified problem, where the middle layer has a much smaller viscosity than the liquid films. Denoting the real part of the exact growth rates by $\mathrm{Re}(\sigma_+^e)$ and $\mathrm{Re}(\sigma_-^e)$, the relative error of the simplification is defined by

$$\Delta\sigma_{\pm}^2 = \frac{\displaystyle\int_0^{k_{\max}} \left[\mathrm{Re}(\sigma_{\pm}^e) - \mathrm{Re}(\sigma_{\pm})\right]^2 \mathrm{d}k}{\displaystyle\int_0^{k_{\max}} \left[\mathrm{Re}(\sigma_{\pm}^e)\right]^2 \mathrm{d}k}. \tag{23}$$

The linearly neutrally stable wavenumber ($k_{\max} = \sqrt{2}k_{\mathrm{char}}$ with k_{char} defined by (16)) is taken as the limit of the integrals, as one is mainly interested in the regime of unstable wavenumbers ($k < k_{\max}$), for which $\mathrm{Re}(\sigma_+) \geq 0$. After substituting the expressions for the growth rates into (23), one finds that $\Delta\sigma_{\pm}^2$ are independent of the Reynolds and the capillary number. This is an important property, as it shows that even though the growth rates are functions of $Re\sqrt[3]{Ca}$, the error introduced by the assumption of semi-rigidness is only a function of the viscosity, density ratios, and H_0. For instance, this implies that after its validity has been verified for a given setup, semi-rigidness remains a valid assumption even if some of the system parameters, such as the flux of the gas flow, are changed. An example of the results for a water–air system is depicted in Fig. 4. Values for the material properties at 25 °C and 1 bar used to generate this figure are summarized in Table 2.

Figure 4 confirms intuition in the sense that the assumption of semi-rigidness becomes less accurate with increasing the blockage of the total channel width by the liquid films. For the examples shown, this is particularly noticeable for $H_0 \geq 0.11$. While approximations estimating the accuracy of the assumption of semi-rigidness are only valid for the equations linearized in η_1 and η_2, one does not expect the order of the relative error to change considerably for the nonlinear equations. This can be explained by the linearity of the viscous stress term in the Navier–Stokes equation.
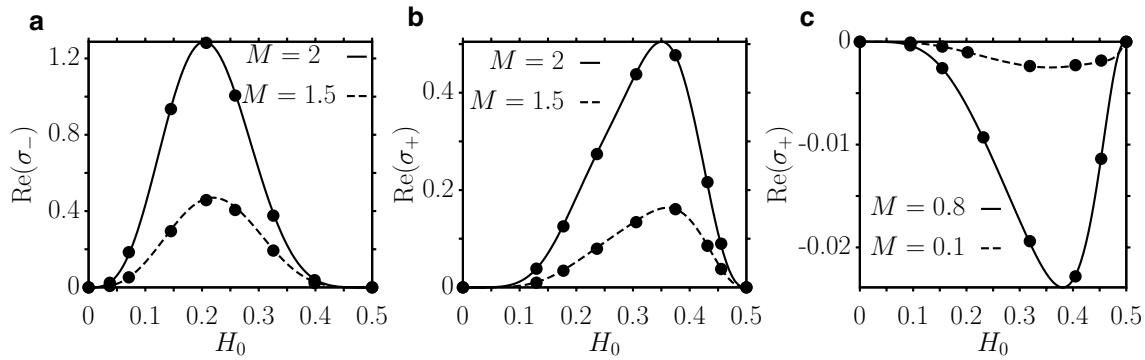
Fig. 3 Comparison of the growth rates of the symmetric σ_+ and the antisymmetric σ_- mode, according to expressions (39) and (40), with the numerical results of Renardy (1987). The dots represent the numerical results, which are taken from Figures 2, 4 and 3, respectively, of the referred paper. The lines correspond to the analytical formulas: [$\mu_1 = \mu_3 = 1.56605 \times 10^{-6}$ Pa s, $d = 200\,\mu$m, $\rho_1 = \rho_2 = \rho_3 = 1$ kg m^{-3}, $\partial p / \partial x = 19.62$ Pa m^{-1}, $\gamma \to 0$ (see Appendix 2 for explanation), $k = 0.01/H_0$]

Table 2 Material properties of air, water (Lide and Haynes 2010), and 10 cSt silicone oil (VanHook et al. 1997) for different temperatures at 1 bar pressure

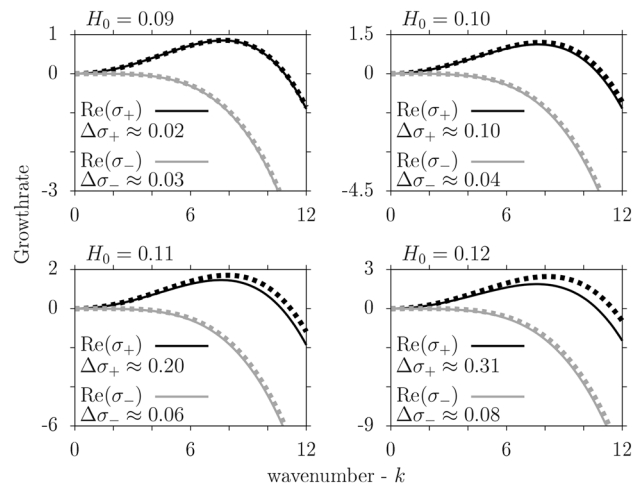| $T = 25\,°C$	
Air	
Parameter	Value
Density	1.161 kg m^{-3}
Viscosity	18.54 × 10^{-6} Pa s
Water	
Density	997.05 kg m^{-3}
Surface tension	71.99 × 10^{-3} N m^{-1}
Viscosity	8.9 × 10^{-4} Pa s
$T = 50\,°C$	
Air	
Parameter	Value
Density	1.089 kg m^{-3}
Viscosity	19.49 × 10^{-6} Pa s
Oil	
Density	940 kg m^{-3}
Surface tension	19 × 10^{-3} N m^{-1}
Viscosity	9.59 × 10^{-3} Pa s

Fig. 4 Real part of the eigenvalues, σ_+ and σ_-, for the linearized water–air system as a function of the wavenumber. The continuous lines indicate the results obtained under the assumption of semi-rigidness of the films ($M \gg 1$), while the exact eigenvalues for the actual value of M are plotted with dashed lines. The initial thickness $H_0 = h_0/d$ of the symmetric liquid films is varied for each plot, as indicated ($d = 200\,\mu$m, mean air velocity 1 m s^{-1}, $Re \approx 10$, $Ca \approx 0.56$)

3.2 Weakly nonlinear analysis

As the eigenvectors of the linear equations v_+ and v_- form a complete set for the function space of possible solutions, one can assume without loss of generality that the solutions of the weakly nonlinear equations take the form

$$\begin{pmatrix} \eta_1 \\ \eta_2 \end{pmatrix} = \int_{-\infty}^{\infty} \left[A_+(k, \tau) v_+ e^{\sigma_+ \tau} + A_-(k, \tau) v_- e^{\sigma_- \tau} \right] e^{ikX} dk. \quad (24)$$

This expression is formally identical to the one presented in Eq. (15), except that here the Fourier coefficients are not only functions of the wavenumber k but are also time-dependent. This occurs due to the mixing of the linear modes through the nonlinear terms of the evolution equations. The growth rates $\sigma_\pm$ are still defined by the same expressions as in Eq. (15). After substituting this integral into Eqs. (13) and (14), one obtains the relationships between the Fourier coefficients to be given by

$$\frac{\partial A_+}{\partial \tau}e^{\sigma_+ \tau} + ik\left[\frac{3(1+6H_0)}{(1-2H_0)^5}(A_+e^{\sigma_+ \tau}) \underset{k}{*} (A_+e^{\sigma_+ \tau})\right.$$
$$\left. + \frac{3(1+2H_0)}{(1-2H_0)^3}(A_-e^{\sigma_- \tau}) \underset{k}{*} (A_-e^{\sigma_- \tau})\right] = 0,$$
$$\frac{\partial A_-}{\partial \tau}e^{\sigma_- \tau} + ik\frac{6(1+4H_0)}{(1-2H_0)^4}(A_+e^{\sigma_+ \tau}) \underset{k}{*} (A_-e^{\sigma_- \tau}) = 0, \tag{25}$$

where $f \underset{k}{*} g := \int_{-\infty}^{\infty} f(k-k')g(k')\mathrm{d}k'$ is the convolution of the functions with respect to the wavenumber. The derivation of these equations is discussed in detail in Appendix 3. For the calculations and the discussion of the actual film deformations, it is useful to introduce the variables

$$\zeta_+(\xi,\tau) = \int_{-\infty}^{\infty} A_+ \exp[\mathrm{Re}(\sigma_+)\tau + ik\xi]\,\mathrm{d}k$$
$$\zeta_-(\xi,\tau) = \int_{-\infty}^{\infty} A_- \exp[\mathrm{Re}(\sigma_-)\tau + ik\xi]\,\mathrm{d}k. \tag{26}$$

Since, in the definition of ζ_- and ζ_+, the imaginary parts of the growth rates were omitted, one needs to consider them as a shift along the spatial coordinate. Formally, the film deformations are given by

$$\eta_1(X,\tau) = \zeta_+(X - 6H_0/\big[\epsilon(1-2H_0)^4\big]\tau,\tau)$$
$$+ \zeta_-(X - 6H_0/\big[\epsilon(1-2H_0)^3\big]\tau,\tau), \tag{27}$$

$$\eta_2(X,\tau) = \zeta_+(X - 6H_0/\big[\epsilon(1-2H_0)^4\big]\tau,\tau)$$
$$- \zeta_-(X - 6H_0/\big[\epsilon(1-2H_0)^3\big]\tau,\tau), \tag{28}$$

i.e., ζ_+ and ζ_- define the magnitude of the symmetric and the asymmetric deformations at a point along the horizontal coordinate. An inverse Fourier transformation of Eq. (25) results in the partial differential equations

$$0 = \frac{\partial \zeta_+}{\partial \tau} + \frac{H_0^3}{3}\frac{\partial^4 \zeta_+}{\partial \xi^4} + Re\sqrt[3]{Ca}\frac{6}{35}\frac{H_0^2(1+4H_0)}{(1-2H_0)^3}\frac{\partial^2 \zeta_+}{\partial \xi^2}$$
$$+ \frac{3(1+6H_0)}{(1-2H_0)^5}\frac{\partial \zeta_+^2}{\partial \xi} + \frac{3(1+2H_0)}{(1-2H_0)^3}\frac{\partial \zeta_-^2}{\partial \xi}\bigg|_{\xi + \frac{12H_0^2}{\epsilon(1-2H_0)^4}\tau}, \tag{29}$$

$$0 = \frac{\partial \zeta_-}{\partial \tau} + \frac{H_0^3}{3}\frac{\partial^4 \zeta_-}{\partial \xi^4}$$
$$+ \frac{6(1+4H_0)}{(1-2H_0)^4}\frac{\partial \left[\zeta_-\left(\zeta_+\big|_{\xi - \frac{12H_0^2}{\epsilon(1-2H_0)^4}\tau}\right)\right]}{\partial \xi}. \tag{30}$$

The subscript $X \pm 12H_0^2/[\epsilon(1-2H_0)^4]\tau$ represents the differences in the phase velocities of the symmetric and the antisymmetric mode. It indicates that one evaluates the corresponding function at a shifted value of X. For verification, the expressions of Eqs. (27) and (28) may be substituted directly into Eqs. (13) and (14). This has been found to also lead to Eqs. (29) and (30). Note that all terms of the derived equations are $O(\epsilon^0)$. This has been obtained by a fundamentally different approach than the one used in the previous studies. Those were limited to systems for which the application of a Galilean transformation was sufficient to avoid terms scaling with different orders of ϵ in the governing equations (Papaefthymiou et al. 2013). Herein, such a transformation would have been impractical as the velocities of the two modes are not identical. This is apparent from Eqs. (27) and (28). It is noted that due to the vastly different viscosity ratios of the systems discussed in other related works (Papaefthymiou et al. 2013; Kliakhandler and Sivashinsky 1995), no direct comparison between the results is possible. Furthermore, as the work of Papaefthymiou and Papageorgiou (2017) focuses on inertialess multilayer systems with negligible surface tension, their results are also not applicable for the present study.

The equations show that, while the (weakly nonlinear) symmetric deformation is affected by the inertial flow, the antisymmetric mode is not influenced by it directly. Furthermore, by introducing the variables ζ_+ and ζ_-, the advective terms of Eqs. (13) and (14) transform into a nonlocal coupling effect between the instability modes. To describe this coupling, it is useful to transform the equations. Similar to the approach used to analyze the Kuramoto–Sivashinsky equations (Chang and Demekhin 2002), one multiplies Eqs. (29) and (30) with ζ_+ and ζ_-, respectively, and integrates the resulting equations along $-\infty < \xi < \infty$. Assuming that, for every τ, the deformations and their derivatives vanish as $\xi \to \pm\infty$ (i.e., at a fixed point in time, the interfaces are pinned at $X \to \pm\infty$ with a contact angle of 90°), one finds that

$$0 = \frac{\partial}{\partial \tau}\left\langle \zeta_+^2 \right\rangle + \frac{2H_0^3}{3}\left\langle \left(\frac{\partial^2 \zeta_+}{\partial \xi^2}\right)^2 \right\rangle$$
$$- Re\sqrt[3]{Ca}\frac{12}{35}\frac{H_0^2(1+4H_0)}{(1-2H_0)^3}\left\langle \left(\frac{\partial \zeta_+}{\partial \xi}\right)^2 \right\rangle$$
$$- \frac{6(1+2H_0)}{(1-2H_0)^3}\mathrm{corr}\left(\frac{\partial \zeta_+}{\partial \xi}, \zeta_-^2\right)\bigg|_{\frac{12H_0^2}{\epsilon(1-2H_0)^4}\tau}, \tag{31}$$

$$0 = \frac{\partial}{\partial \tau}\left\langle \zeta_-^2 \right\rangle + \frac{2H_0^3}{3}\left\langle \left(\frac{\partial^2 \zeta_-}{\partial \xi^2}\right)^2 \right\rangle$$
$$+ \frac{6(1+4H_0)}{(1-2H_0)^4}\mathrm{corr}\left(\frac{\partial \zeta_+}{\partial \xi}, \zeta_-^2\right)\bigg|_{\frac{12H_0^2}{\epsilon(1-2H_0)^4}\tau}, \tag{32}$$

where $\mathrm{corr}\left(\dfrac{\partial \zeta_+}{\partial \xi}, \zeta_-^2\right)\Big|_{\Delta\xi} = \int_{-\infty}^{\infty} \dfrac{\partial \zeta_+}{\partial \xi}\Big|_{\xi} \zeta_-^2\Big|_{\xi+\Delta\xi}\, d\xi$ denotes the

correlation function. The equations remain the same if—instead of the condition of pinned interfaces—periodic boundary conditions are applied at the domain boundaries. The operator $\langle f(\xi)\rangle$ represents the integration of $f(\xi)$ on $[-\infty, \infty]$. The quantities $\langle \zeta_+^2\rangle$ and $\langle \zeta_-^2\rangle$ characterize the magnitude of the symmetric and the antisymmetric instability mode, respectively, over the whole length of the interface. As $\langle(\partial\zeta_+/\partial\xi)^2\rangle$ is nonnegative, the perturbation due to the inertial term always leads to an increase of the symmetric deformations. Similarly, $\langle(\partial^2\zeta_+/\partial\xi^2)^2\rangle$ is always nonnegative as well, so that capillarity always decreases the deformation amplitudes. Therefore, the interfaces are not susceptible to capillary-induced instabilities. The absence of such instabilities in the system is discussed in more detail in Appendix 4.

As summarized in Appendix 5, from numerical simulations, it was found that the antisymmetric mode is always dampened out. Intuitively, this can be understood as follows: Eqs. (31) and (32) suggest that the antisymmetric instability mode can only be destabilized if the correlation function between the antisymmetric and the symmetric modes is negative. In this case, Eq. (31) indicates that $\langle \zeta_+^2\rangle$ grows slower than for configurations for which the correlation is positive. In turn, for a positive correlation function, the symmetric deformation further dampens the antisymmetric instability. Thus, one expects the symmetric instability mode to have a generally stabilizing effect on the antisymmetric one. Moreover, as $\tau \to \infty$, the spatial distance over which the correlation is evaluated also tends to infinity. Although dissipative systems are known to exhibit long-range coherent behavior (Nicolis and Prigogine 1977), the correlation function still needs to vanish in physically realistic setups as the shift between ζ_+ and ζ_- tends to infinity. Therefore, after sufficiently long time, the coupling between the instability modes will have a negligible effect on the film evolution. Both arguments, supported by numerical tests, suggest that the antisymmetric instability mode decays during the long-time evolution of the interfaces, which can be formally expressed by $\langle \zeta_-^2\rangle \to 0$, and thus, $\zeta_- \to 0$ at every point. Hence, as long as the symmetric mode is unstable, one may assume that as time proceeds $\zeta_- \ll \zeta_+$. From this and Eq. (29), one can deduce that the physically relevant symmetric instability mode will evolve according to the Kuramoto–Sivashinsky equation given by

$$0 = \frac{\partial \zeta_+}{\partial \tau} + \frac{H_0^3}{3}\frac{\partial^4 \zeta_+}{\partial \xi^4} + Re\sqrt[3]{Ca}\,\frac{6}{35}\frac{H_0^2(1+4H_0)}{(1-2H_0)^3}\frac{\partial^2 \zeta_+}{\partial \xi^2}$$
$$+ \frac{3(1+6H_0)}{(1-2H_0)^5}\frac{\partial \zeta_+^2}{\partial \xi}, \tag{33}$$

which is noted to be independent of the parameter ϵ. This implies that although the initial behavior of the system is affected by this parameter, it only influences the dimensionless velocity of the emerging waves at large times according to Eqs. (27) and (28). Substituting the definition of Eqs. (27) and (28) permits to transform this equation into evolution equations of η_1 and η_2. Nonlinear partial differential equations of this type have been first derived for reaction–diffusion systems (Kuramoto and Tsuzuki 1976) and for liquid-film instabilities (Sivashinsky and Michelson 1980). They have been the subject of extensive analytical (Chang and Demekhin 2002; Kudryashov 1990) and numerical studies (Cvitanovic et al. 2010; Kevrekidis et al. 1990). Therefore, the further analysis of these equations will not be discussed here in detail; the reader is referred to the existing literature on the topic.

After calculating ζ_+ with Eq. (33) (under the assumption that the coupling to the antisymmetric mode is negligibly small), one can solve Eq. (30) independently to obtain ζ_-. It is noted that even when ζ_- is not negligibly small compared to ζ_+, Eqs. (29) and (30) are still reducible to a single evolution equation. The derivation of this quite complicated equation is discussed in Appendix 6.

In the long-time limit, equations of the form

$$\frac{\partial u}{\partial t} + \nu\frac{\partial^4 u}{\partial x^4} + \frac{\partial^2 u}{\partial x^2} + \frac{1}{2}\frac{\partial u^2}{\partial x} = 0 \tag{34}$$

should have a bounded solution (Hyman and Nicolaenko 1986), where an upper bound scales like $\nu^{-1/4}$. After rescaling of Eq. (33) to take the same form as Eq. (34), this condition transforms to

$$\lim_{\tau\to\infty}\sup(\zeta_+) \le \beta\left[\frac{(1+6H_0)^2}{H_0^3(1-2H_0)(1+4H_0)^3 CaRe^3}\right]^{-1/4}.\tag{35}$$

Therefore, the amplitudes of the interfacial deformation cannot increase indefinitely, but should be stabilized by the nonlinear terms in the evolution equation. While this property is consistent with physical intuition, giving an exact upper limit for the deformation amplitudes is not possible due to the unknown constant β on the right-hand side of the expression.

As mentioned above, to examine the long-term damping of the antisymmetric instability mode, a number of simulations of the full evolution equations [Eqs. (7) and (8)] were conducted. The finite-element method with quadratic (Lagrangian) shape functions was applied for solving the equations. The calculations were performed with Comsol (2014) using the Matlab Livelink environment. The dimensionless parameters were varied according to $H_0 \in [0.01, 0.3]$, $\epsilon \in [0.01, 0.5]$, $Re \in [1, 50]$, and $Ca \in [0.125, 5]$. The simulation results are summarized in

Appendix 4. They all indicate that the antisymmetric mode is quickly damped out. Thus, for symmetric systems, the films fully synchronize in phase and amplitude.

An example of the evolution of $\langle \zeta_-^2 \rangle$ and $\langle \zeta_+^2 \rangle$ is depicted in Fig. 5. As for all of the simulations conducted, the length of the simulated domain was $L = 40\pi/k_{char}$ with periodic boundary conditions. This corresponds to a sampling rate of $k_{char}/20$ in Fourier space. The length was divided into 200 cells. Hence, according to the Nyquist theorem, the maximal numerically resolvable wavenumber would be $5k_{char}$ if the domain was discretized with a finite-different scheme. The finite-element discretization with quadratic Lagrangian shape functions utilized for the simulations exceeds this resolution. In any case, although the strong nonlinearity of the evolution equations suggests that higher wavenumbers than $k_{max} = \sqrt{2}k_{char}$ should also appear during the evolution, the highest unstable wavenumber in the full nonlinear simulations was still found to be considerably smaller than $5k_{char}$. As an initial condition, the interfaces were assumed to be flat except for a small white-noise perturbation with an amplitude of $0.01H_0$ added to the surface of the lower film. Since the upper film was initially undeformed ($\eta_2 = 0$), it was ensured that at the beginning $\langle \zeta_-^2 \rangle = \langle \zeta_+^2 \rangle$.

For the simulations referred to in Fig. 5, silicone oil (10 cSt) and air at a temperature of 50 °C and at 1 bar pressure were assumed as the working fluids. Their material properties are summarized in Table 2. The undisturbed film thicknesses were $H_0 = 0.2$, which corresponds to an error of $\Delta\sigma_+ \approx 0.005$ and $\Delta\sigma_- \approx 0.006$ in the (linear) growth rates caused by the truncation of the viscosity-ratio expansion [see Eq. (23)]. Therefore, for this configuration, the assumption of semi-rigid liquid films is valid. The channel width was set to $d = 200$ μm, and the mean air-flow velocity was assumed to be 3.5 m s^{-1}. The corresponding Reynolds and capillary numbers are $Re \approx 23.46$ and $Ca \approx 0.15$, while $\epsilon \approx 0.12$. The maximal deformation of the interfaces was found to be $\Delta H \approx 0.028$; thus, the relative contribution to the pressure field due to inertia was approximately 0.23 according to Eq. (22). Hence, all assumptions necessary for the validity of Eqs. (7) and (8) were fulfilled during the simulation.

Plot (a) of Fig. 5 shows the interface shapes at $\tau = 1$, while plot (b) depicts the spectrum of the absolute values of the Fourier coefficients of the symmetric deformation, ζ_+, at the same time instance. From this plot, one can deduce that there is no well-defined characteristic (i.e., dominating) wavelength of the instability, which is a consequence of the pronounced nonlinearity of the evolution equations. Similarly, while high wavenumbers are damped, the nonlinearity of Eqs. (7) and (8) implies that wavenumbers larger than k_{max} (obtained from the linear analysis) are unstable, as well. This does not cause any problems in the simulations, as the largest appearing wavenumber is still much smaller than the resolution of the mesh, $5k_{char}$.
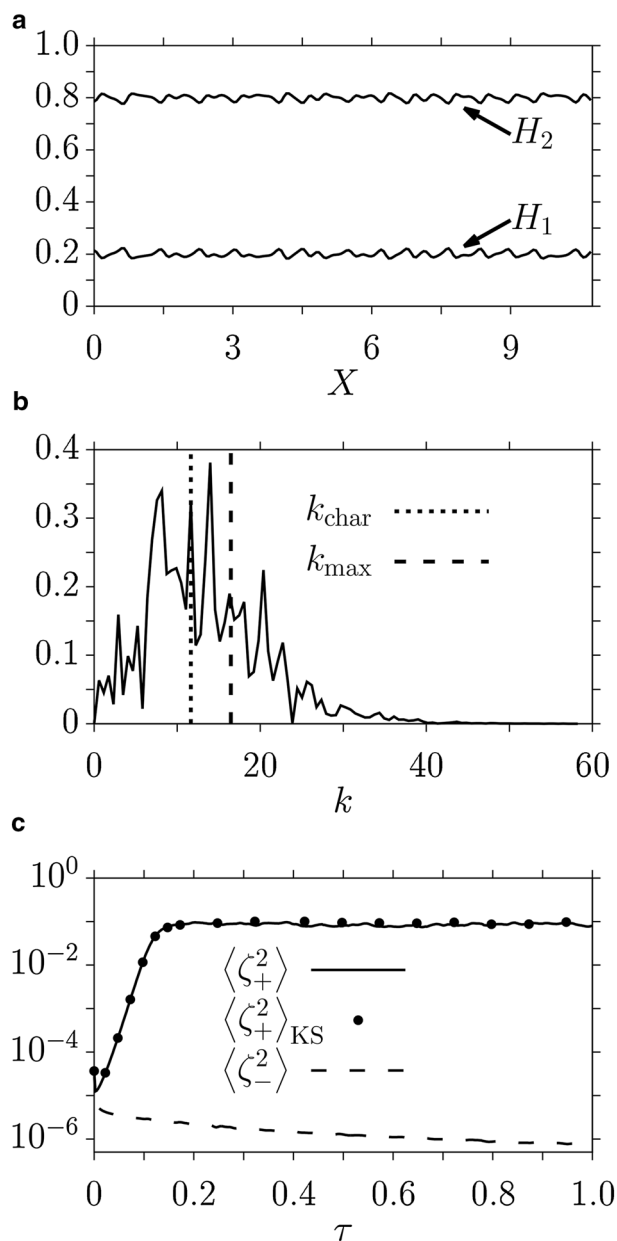
Fig. 5 Example for the numerical results obtained by solving (7) and (8) for $H_0 = 0.2$, $Re = 23.46$, $Ca = 0.15$, and $\epsilon = 0.12$. Plot **a** shows the interfaces along the channel at $\tau = 1$, **b** depicts the absolute values of the Fourier coefficients of ζ_+ at $\tau = 1$. The values of k_{max} and k_{char} correspond to the two dashed vertical lines. Plot **c** shows the time evolution of the symmetric and the antisymmetric instability mode. The approximate solution according to the Kuramoto–Sivashinsky (KS) equation is shown for comparison

Figure 5c shows the time evolution of $\langle \zeta_+^2 \rangle$ and $\langle \zeta_-^2 \rangle$. As one expects, the antisymmetric instability mode is damped quickly, and $\langle \zeta_+^2 \rangle$ becomes much larger than $\langle \zeta_-^2 \rangle$ after a short initial transition period. For comparison, a simulation of the Kuramoto–Sivashinsky equation [Eq. (33)] was also performed. As the initial condition, the initial distribution of ζ_+ from the previous simulation was utilized (i.e., the

initial white-noise distribution is identical). One finds that the graph of $\langle \zeta_+^2 \rangle$ obtained from the simulation of the full evolution equations [Eqs. (7) and (8)] is essentially identical to the one calculated from the simplified problem $\langle \zeta_+^2 \rangle_{KS}$. This comparison was also performed for three other systems. For the first one, all parameters were the same as in Fig. 5, but the mean air velocity was changed to $u = 5 \, \text{m s}^{-1}$. Similarly, for the second and third simulation, the governing parameters were unchanged, except that the nondimensional film thickness was $H_0 = 0.1$ and the channel width was $d = 100 \, \mu\text{m}$, respectively. For all the cases, the simplified equation was found to provide a good approximation of the behavior of the full system, even at early times. The accuracy of the approximation is comparable to what is shown in Fig. 5c. Thus, these results verify numerically that Eq. (33) accurately approximates the time evolution of the original nonlinear equations, Eqs. (7) and (8).

Returning to the question posed at the beginning of Sect. 3, one may conclude that the mirror symmetry of the system does not break down dynamically. Even if the fluctuations along the interfaces are not symmetric, they do not give rise to a self-sustaining asymmetric deformation of the interfaces. This can intuitively be understood by the mechanism explained in the context of Fig. 2: An initial thickness disturbance on one film will lead to pressure fluctuations and shear stress variations along the surface of the other film. They act in a direction that always fosters a deformation of that film not only at the same location and in the same direction as the initial disturbance but—given the identical initial thickness of both films—also of the same amplitude. Since this mechanism applies to all thickness disturbances, the evolutions of both films are completely synchronized. However, it should be noted that such an intuition is only correct if the liquid films are much more viscous than the fluid in between. Indeed, if the viscosity ratio M is not sufficiently large, then both the symmetric and the antisymmetric mode can become unstable, so that this conclusion does no longer hold. This is apparent from the formulas for the corresponding (linear) growth rates given in Appendix 2. Hence, the initial symmetry alone does not ensure a fully synchronized evolution of both films.

Less intuitive is the finding that the coupled system becomes more unstable than the isolated films under identical base flow conditions, as indicated by the enlarged wavenumber of the fastest growing mode in the linear theory. In the weakly nonlinear regime, the saturation deformation amplitude is seen to be affected by the coupling, as well. However, in light of the complex and partially unknown properties of the Kuramoto–Sivashinsky equation, no upper bound can be given for this quantity, neither for the single nor for the double film system. Therefore, the magnitude of the coupling effect on that parameter cannot be quantified, in general.

4 Asymmetric systems

In realistic systems, complete mirror symmetry of the undisturbed system is not a valid assumption. For broken symmetry, it is possible to perform a second perturbation analysis for the deviation from the symmetric configuration. Nevertheless, to get a qualitative overview of systems with high asymmetry, it is favorable to use numerical calculations. For this purpose, the initial thicknesses of the liquid films are allowed to differ by a nondimensional quantity δ, which defines the difference between the initial thicknesses of the undisturbed films according to

$$H_1(t = 0) = H_0(1 + \delta/2),$$
$$H_2(t = 0) = H_0(1 - \delta/2), \quad \delta \in [0, 2). \tag{36}$$

The goal of the present analysis is to find how the coupling between the two films changes with δ. For this purpose, the evolution of the liquid films was simulated with the same numerical method as introduced in the previous section. Furthermore, the quantities used for nondimensionalization were defined in the same way as for symmetric systems. Given that the evolution of the film thicknesses is still described by Eqs. (7) and (8), the dynamics of the interfaces should be only governed by the four dimensionless numbers, ϵ, $Re \sqrt[3]{Ca}$, H_0, and δ.

To quantify the coupling strength between the layers, the normalized correlation of the interface deformation amplitudes ΔH_1 and ΔH_2 is defined by

$$C(\tau) = \frac{\int\limits_{-\infty}^{\infty} \Delta H_1(\tau, X) \Delta H_2(\tau, X) \, dX}{\sqrt{\int\limits_{-\infty}^{\infty} \Delta H_1^2(\tau, X) \, dX \int\limits_{-\infty}^{\infty} \Delta H_2^2(\tau, X) \, dX}}. \tag{37}$$

A convenient property of C is that it is invariant under the transformation $\Delta H_1 \to \alpha_1 \Delta H_1$, $\Delta H_2 \to \alpha_2 \Delta H_2$ as long as $\alpha_1 \times \alpha_2$ is positive and independent of X. Thus, even if the magnitudes of the deformations are different, the normalized correlation function may remain the same. This is useful, since one expects the thinner film to have a smaller deformation than the thicker one. For phase-synchronized deformations, $C = 1$, while $C = 0$, if the film deformations are uncorrelated. At the $C = -1$ limit, the interfaces are in antiphase, i.e., $\Delta H_1 = -\alpha \Delta H_2$, where $\alpha > 0$ is independent of X.

All simulations indicate that, at $\delta = 0$, the correlation function tends to unity as $\tau \to \infty$. For symmetric systems, this is to be expected, since—as discussed above—in those cases, the antisymmetric mode disappears in the long-time limit. Hence, for symmetric systems, $\Delta H_1 \approx \Delta H_2$ after a sufficiently long-time period. Relative to the symmetric case, the correlation is seen to decrease with increasing values of δ. A number of simulations were

performed for the dimensionless parameters $H_0 \in [0.04, 0.2]$, $Re\sqrt[3]{Ca} \in [1, 10]$, $\delta \in [0, 1.999]$, and $\epsilon \in [0.01, 0.125]$. The value of C was found to be nonnegative in all the cases studied. Consequently, even for the asymmetric configuration, the deformations of the two films have predominantly the same sign.

In Fig. 6, examples of the evolution of the correlation function with δ are shown. Once again, the silicone oil of Table 2 was considered as the liquid medium, while air was chosen for the intermediate gas layer. For the first set of simulations, the channel thickness was $d = 50\ \mu m$. The dimensionless initial liquid-layer thicknesses at $\delta = 0$ were $H_0 = 0.04$, and the mean air velocity was $u = 5\ m\,s^{-1}$. For the second and third sets of simulations, these parameters were $d = 50\ \mu m$, $H_0 = 0.08$, $u = 5\ m\,s^{-1}$ and $d = 100\ \mu m$, $H_0 = 0.15$, $u = 3\ m\,s^{-1}$, respectively. For the last set of simulations, the values were $d = 100\ \mu m$, $H_0 = 0.2$, $u = 3\ m\,s^{-1}$. In dimensionless coordinates, the channel length was set to 20, while it was divided into at least 500 cells to ensure grid independence. The time evolution of $\langle \Delta H_1^2 \rangle$ and $\langle \Delta H_2^2 \rangle$ strongly resembles the graph of $\langle \zeta_+^2 \rangle$ in Fig. 5c). Therefore, for the current analysis, the simulated time interval after which C was evaluated was chosen to be long enough to ensure that the values of $\langle \Delta H_1^2 \rangle$ and $\langle \Delta H_2^2 \rangle$ only oscillated around their asymptotic value in the last 10% of the time interval. The corresponding dimensionless time was 1600 in the first, 1000 in the second, 160 in the third and 120 in the fourth set of simulations. These correspond to approximately 849 s, 822 s, 977 s, and 909 s in real time. It is noted that the highest value of δ for the last set of simulations was 1.7 due to the increase in the computational requirements of the calculations with δ and H_0. The correlation function was calculated as the average of the correlation between the film thicknesses in the final 10% of the simulated time interval.
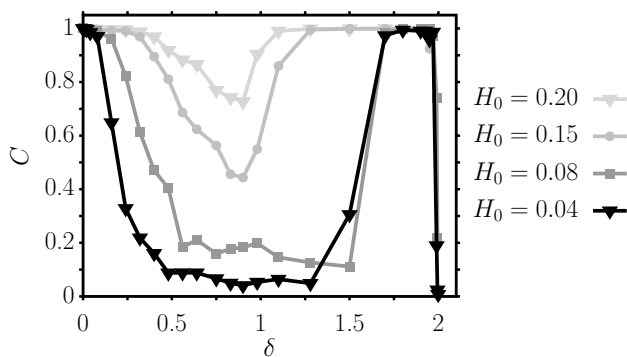
All simulations show similar characteristics. Initially, the correlation function decreases with increasing values of δ. This was found to be a consequence of a very slowly emerging instability of the thinner liquid layer, detuning the two interfaces. As δ further increases, this process either disappears or its growth rate becomes small enough to no longer affect the patterns within the simulated time interval, leading to an increase of the correlation between the films. At $\delta \approx 2$, when the ratio of the undisturbed film thicknesses is about 100, C drops sharply. This is not a surprising result, since, at this point, the order of magnitude of the terms in the evolution equations [Eqs. (7) and (8)] is very different for each film, and one does no longer expect the layers to have a qualitatively similar behavior. The unevenness of the curves is a consequence of the small, δ-dependent rate of the detuning. Given that obtaining a single data point took in some cases several days to compute, performing longer simulations was generally not possible due to limitations in computational resources. Therefore, it is presumed that the simulated time interval was not sufficiently large to capture the full development of the detuning for all simulations. In these cases, the correlation function may not have reached its stationary value. However, the behavior of the system is not a numerical artifact: the spectrum of unstable wavenumbers of the interfacial deformations stayed within the range of the numerical resolution of the simulations, and no rapid temporal variations emerged during the calculations.

Notably, the correlations of most systems were close to unity for $\delta \in [0, 2]$ for several minutes. This result indicates that, even in a highly asymmetric system, one may often utilize the assumption that at the initial stages of their development the patterns on the two interfaces are identical apart from a constant factor between their amplitudes. For highly asymmetric systems, the deformation of the thinner film is expected to have a smaller effect on the pattern of the thicker film than vice versa. Therefore, at high values of δ, where $C \approx 1$, this indicates that the deformation of the thinner film is enslaved by the instability of the thicker one.

To a certain degree, the synchronization of the interfaces can be explained qualitatively by examining the linear properties of the system. For this purpose, one considers the uncoupled liquid layers, i.e., similarly as for Eq. (21), it is assumed that only the thicker (thinner) liquid layer may deform, while the deformation of the thicker (thinner) liquid interface is suppressed. By performing a linear stability analysis for these systems, one may obtain the characteristic length scales of the patterns that would emerge on the interfaces if the deformations of the two interfaces did not affect each other. The calculation is straightforward, and Fig. 7 depicts the normalized characteristic wavenumber for the thinner and the thicker liquid layer for a set of parameters. These plots show that even up to $\delta = 1.5$, for which the lower film is seven times thicker than the upper
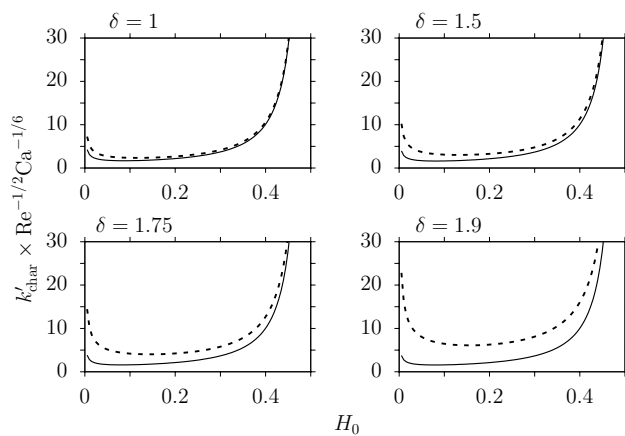

Fig. 6 Dependence of the correlation function C on the thickness difference δ for systems with different nominal film thicknesses H_0. (The velocities and channel thicknesses for $H_0 = 0.2$ were $u = 3\ m\,s^{-1}$ and $d = 100\ \mu m$. For $H_0 = 0.15$, they were $u = 3\ m\,s^{-1}$, $d = 100\ \mu m$; for $H_0 = 0.08$: $u = 5\ m\,s^{-1}$, $d = 50\ \mu m$; and for $H_0 = 0.04$: $u = 5\ m\,s^{-1}$, $d = 50\ \mu m$)

Fig. 7 Normalized characteristic wavenumber of the uncoupled layers for different values of δ and H_0

one, the characteristic wavenumbers of the two interfaces are very similar. The difference between the characteristic length scales increases with decreasing H_0 and increasing δ. This implies that, for a large range of parameters, the deformational wavelengths would be comparable, even if the interfaces were uncoupled. For the coupled system, Eqs. (9) and (10) show that both the pressure drop and the viscous stresses destabilizing the layers are more prominent if the two interfaces deform in phase with each other. Therefore, if the characteristic length scales of the emerging patterns of the uncoupled interfaces are comparable, even a weak coupling is sufficient to promote their synchronization. If these quantities are principally different, a stronger coupling would be necessary to synchronize the two interfaces. Therefore, one expects the correlation function to decrease for $\delta \rightarrow 2$ as well as for $H_0 \rightarrow 0$, which agrees with the results of Fig. 6. The increase of the correlation function near $\delta = 1$ and beyond is presumably a consequence of the very slow self-patterning of the thinner liquid layer, combined with its coupling to the rapid pattern formation process of the thicker layer. At $\delta = 1$, the linear analysis shows that the growth rate of the most unstable wavenumber is about an order of magnitude larger for the uncoupled thicker layer in comparison with the thinner one. At $\delta = 1.9$, it is generally more than two orders of magnitude larger.

5 Conclusion

In this paper, the hydrodynamic coupling between the long-wavelength instabilities emerging at the interfaces of thin liquid films, which cover the walls of a plane-parallel microchannel and are exposed to a gaseous flow along the channel center plane, has been investigated. To the best of our knowledge, this setup has not been analyzed in detail

in the previous studies, despite its practical relevance. The governing equations were simplified by employing the long-wavelength approximation and by assuming moderate values for the Reynolds number. The small viscosity ratios of the gaseous to the liquid media were utilized to simplify the system further, so that it can be described and analyzed by two relatively compact evolution equations. The fully and weakly nonlinear forms of the governing equations correspond to the expectations based on the previous analyses. While Papaefthymiou et al. (2013) treated similar systems numerically, the discussion of the current study is focused on the analytical characterization of the unstable modes of the system. In contrast to the analytical results of Papaefthymiou and Papageorgiou (2017), employing substantially different physical assumptions, inertia and surface tension effects were accounted for.

Based on the simplified model, it was shown that, for initially symmetric films on both walls (i.e., identical material properties and initial thicknesses), the interface deformations can be described by the superposition of a symmetric and a linearly independent antisymmetric mode. It was found that the interfaces are not destabilized by capillary forces, agreeing with the implications of previous studies. By means of a linear and weakly nonlinear stability analysis, it was found that the symmetric mode is linearly unstable but grows only up to a maximum deflection amplitude. The linear analysis implies that, for liquid films thinner than 1 / 8 of the total channel width, this mode is mainly driven by variations of the viscous stresses along the interfaces. For thicker films, variations in the pressure gradient are the main source of this mode of instability. The weakly nonlinear analysis indicates that the large contribution of the nonlinear terms significantly widens the spectrum of unstable wavenumbers in comparison to the linear regime. A characteristic wavelength clearly dominating the pattern cannot be identified. In contrast to the symmetric mode, the antisymmetric mode is not inherently unstable, but can only exhibit an instability due to its coupling to the symmetric mode. At long times, the antisymmetric mode disappears, so that in the weakly nonlinear regime the system is governed by a single Kuramoto–Sivashinsky equation. This surprising finding stands in contrast to systems addressed in the related studies. It is noted that this result does not necessarily hold if the intermediate layer has an arbitrary viscosity. To verify this, the study provides analytical expressions for the (linear) growth rates for such systems, which were found to be in complete agreement with numerical simulations conducted for selected cases by other researchers. With respect to the hydrodynamic coupling between the two films it was shown that the interaction enhances the degree of instability. Namely, the wavenumber of the fastest growing mode in the linear theory is $\sqrt{2}$ times larger than if both films were to evolve under the

same conditions but isolated from each other. In the weakly nonlinear regime, the maximal deformation amplitude was seen to be affected by the coupling as well.

For asymmetric systems, a numerical and linear analysis has been performed as well. For long elapsed time periods, it was found that the correlation between the interfacial deformations remains close to unity for an extended period of time even for highly asymmetric configurations. This implies that, even for such systems, the patterns of the two interfaces often remain approximately phase-synchronized for a long time. Nevertheless, after much longer than this initial period, the films are expected to detune from each other due to their inherently different patterning processes.

Finally, it is emphasized that the method used for the analysis of this system can be easily generalized to more complex systems. For instance, introducing Marangoni stresses or gravitational forces to the equations will only add a new term to the evolution equations [Eqs. (7) and (8)], but the approach to tackle these problems is essentially the same as the one discussed in this paper. Our findings are relevant for systems where the walls of narrow ducts are coated by thin liquid films, which do not severely obstruct the gas flow in the center. Examples are air flow in respiratory ducts coated with mucus, boiling in microchannels, or the flow of a supersaturated gas in a narrow duct, such that liquid condenses at the channel walls.

Appendix 1: Evolution equations

Herein, the method of obtaining the evolution equations Eqs. (7) and (8) is summarized. At first, the following discussion considers a system where the $1/M^2 \ll 1$ condition is not assumed. In this case, one solves Eqs. (1)–(6) for the zeroth and first order of ϵ separately, and assumes that $(\epsilon Re)^2$, $\epsilon^2 \ll 1$. At $O(\epsilon^0)$, one obtains the solution corresponding to solving the Stokes equation in all layers while neglecting the effect of the capillary pressure (as $Ca = O(1)$, capillary effects enter at $O(\epsilon^1)$). To zeroth order in ϵ, an evolution equation for the film thicknesses can be obtained by utilizing the kinematic boundary conditions [Eq. (6)]. Afterwards, these solutions are applied to obtain the first-order solutions in ϵ for the governing equations. This approach has been applied in many studies, for example to the related problem of liquid stability during spin coating (Reisfeld et al. 1991).

To implement the condition $1/M^2 \ll 1$, one solves all equations arising from the previously summarized method only up to order $1/M$. If higher order terms in the viscosity ratio were also included in the equations, Eq. (7) would take the form

$$
\frac{\partial H_1}{\partial \overline{\tau}} = -\frac{\partial}{\partial \overline{X}} \left\{ \frac{H_1^2(3 + H_1 - 3H_2)}{\epsilon(1 - H_1 - H_2)^3} \right.
$$
$$
+ Re\sqrt{3}Ca \frac{3H_1^2(1 + 5H_1 - H_2)}{35(1 - H_1 - H_2)^3} \left(\frac{\partial H_1}{\partial \overline{X}} + \frac{\partial H_2}{\partial \overline{X}} \right)
$$
$$
\left. + \frac{H_1^3}{3} \frac{\partial^3 H_1}{\partial \overline{X}^3} \right\} - \frac{1}{M} \frac{\partial}{\partial \overline{X}} \left\{ \frac{-6H_1^5 - H_1^6 + H_1^4(3 + 6H_2^2)}{\epsilon(1 - H_1 - H_2)^6} \right.
$$
$$
+ \frac{3H_2^3(-2 + H_2 + H_2^3) + H_1^3(-12 + 42H_2)}{\epsilon(1 - H_1 - H_2)^6}
$$
$$
\left. + \frac{H_1^3 H_2^2(-42 + 8H_2)}{\epsilon(1 - H_1 - H_2)^6} + O(\epsilon^0) \right\}
$$
$$
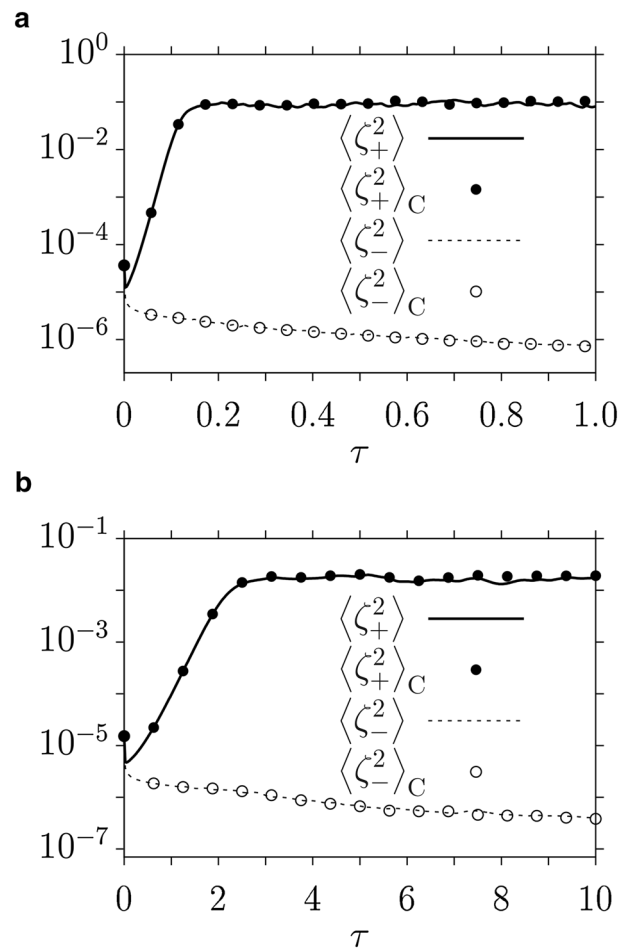+ O\left(\frac{1}{M^2} \right) + \cdots .
$$

(38)

Fig. 8 Evolution of the symmetric instability for **a** silicone oil ($H_0 = 0.2$, $Re = 23.46$, $Ca = 0.15$, $\epsilon = 0.12$, and $1/M = 0.002$) and **b** water ($H_0 = 0.07$, $Re = 37.70$, $Ca = 0.14$, $\epsilon = 0.07$, $1/M = 0.02$) films. The lines correspond to Eqs. (7) and (8); the points to the corrected evolution equations according to Eq. (38)

A similar equation would govern the time evolution of H_2. These equations imply that Eqs. (7) and (8) give a good approximation to the evolution of the system as long as $O(\epsilon) \gg O(1/M)$, in particular if $O(\epsilon^2) \geq O(1/M)$. This corresponds to all the numerical simulations performed for the current paper. It is notable that if $O(\epsilon) \approx O(1/M)$, the additional terms expressed in detail in Eq. (38) would also be necessary for a valid description of the system. However, to the first order in ϵ, these terms would transform to additional linear terms of the weakly nonlinear equations. In this sense, they only modify the first terms on the right-hand side of Eqs. (13) and (14). Especially, for symmetric systems, these terms correspond to the propagation velocity of interfacial waves. As this velocity only affects the coupling term between the symmetric and the antisymmetric instability, it is expected that the main results discussed in the related sections of this paper remain qualitatively valid and quantitatively reasonably accurate even in the $O(\epsilon) = O(1/M)$ regime.

To demonstrate this, Fig. 8 depicts the evolution of the symmetric and antisymmetric instability for a) silicone oil and b) water. The line plots were calculated by evolving the film interfaces according to Eqs. (7) and (8). The point plots correspond to Eq. (38) and to its analogue for H_2. The simulation parameters for Fig. 8a) are the same as used for Fig. 6. Since, in this case $1/M \ll \epsilon$, the two plots match very well, in agreement with the expectations. For the simulation with water films displayed in Fig. 8b), the parameters were chosen as $d = 200$ μm, $H_0 = 0.07$, $u = 3.5$ m/s^{-1}. For this case, according to Eq. (23), the errors of the assumption of semi-rigidness are $\Delta\sigma_+ = 0.08$ and $\Delta\sigma_- = 0.01$. Thus, the parameters are at the limit of the applicability range of the method presented in the paper. Moreover, $\epsilon = 0.07$ and $1/M \approx 0.02$, i.e., they are comparable. Considering these facts, it is especially remarkable that the two sets of graphs remain highly similar. Hence, Eqs. (7) and (8) give a quantitatively good description for the system even in this case, while they remain extremely helpful in retaining a physically understandable picture of the problem. A number of additional simulations indicated that the quantities $\Delta\sigma_+$ and $\Delta\sigma_-$ generally give a good estimate for the validity of semi-rigidness. Performing such a detailed verification of this assumption is considerably more complicated for asymmetric systems. However, intuitively it is still expected that the effects of the additional term in Eq. (38) are overshadowed by the first terms of Eqs. (13) and (14).

Appendix 2: Linear growth rate for arbitrary viscosities

The growth rates from the linear stability analysis of Sect. 3.1 for arbitrary viscosities are given by

$$
\begin{aligned}
\mathrm{Re}(\sigma_+) = {} & \frac{(1 - 2H_0)^2 H_0^2}{210(M - 6(M-1)H_0 + 12(M-1)H_0^2 - 8(M-1)H_0^3)^5} \\
& \times \{k^2 18 Ca^{1/3}(M-1)Re(1 - 2H_0)[2M^4 - 4M^3(-3 + 7M)H_0 \\
& - M^2(-63 + 4(37 - 36M)M)H_0^2 - 6M^2(105 + 4M(-17 + 8M) \\
& - 56R)H_0^3 - 2M(2M(-133 + 12M(-51 + 28M)) + 7(-63 \\
& + 178M)R)H_0^4 - (-756R + 4M(21(60 + 49R) - 2M(1981 \\
& + 4M(-673 + 252M) + 753R)))H_0^5 - 12(21(15 + 7R) \\
& + M(-3255 - 179R + 4M(1743 + 4M(-373 + 112M) \\
& + 44R)))H_0^6 - (48(-420 + 53R) + 16M(7210 - 1027R \\
& + 2M(-5999 + 132(31 - 8M)M + 422R)))H_0^7 - (64(-1 \\
& + M)M(1925 + 28M(-59 + 18M) - 345R) + 96(-1 + M)(-385 \\
& + 97R))H_0^8 - 128(-1 + M)(210 - 54R + M(-595 + 68(7 - 2M)M \\
& + 99R))H_0^9 - 64(-1 + M)(8M(35 - 28M + 8M^2 - 5R) + 5(-21 \\
& + 5R))H_0^{10}] + k^4 35 H_0[(4M - 3)H_0 - 2M][M - 2(M-1)H_0(3 \\
& - 6H_0 + 4H_0^2)]^4\},
\end{aligned}
\tag{39}
$$

$$\mathrm{Re}(\sigma_-) = \frac{H_0^3}{30\mathrm{Ca}^{2/3}(M + 2(1 - M)H_0)^3(M + 2(1 - M)H_0(3 - 6H_0 + 4H_0^2))^2}$$
$$\times \{k^2[18\mathrm{Ca}(-1 + M)Re(1 - 2H_0)H_0(5M^2 + 2M^2(-15$$
$$+ 18R)H_0 + 2M(M(30 - 32R) + 7R)H_0^2 + 4(R - 7MR$$
$$+ 2M^2(-5 + 8R))H_0^3)] + k^4[5\mathrm{Ca}^{2/3}(-2M - (1 - 4M)H_0)(M^2$$
$$- 8(-1 + M)MH_0 + 12(1 - 3M + 2M^2)H_0^2 - 8(3 - 7M$$
$$+ 4M^2)H_0^3 + 16(-1 + M)^2H_0^4)^2]\}, \tag{40}$$

where R is the ratio of the mass densities, defined in Sect. 2.

These formulas were compared with the results of the numerical calculations of Renardy (1987). The corresponding results are summarized in Fig. 3. To match with the nondimensional parameters used in the paper referred to, the material properties were taken as $\mu_1 = \mu_2 = 1.56605 \times 10^{-6}\,\mathrm{Pa\,s}$, $\rho_1 = \rho_2 = \rho_g = 1\,\mathrm{kg\,m^{-3}}$, and a channel width of 200 µm was chosen. Renardy (1987) has performed her numerical calculations for vanishing surface tension, whereas the scaling introduced in the current paper is based on a finite capillary number. For this purpose, the surface tension of the silicone oil listed in Table 2 was used. Subsequently, the effects of the surface tension can be eliminated by omitting the terms in the growth rates (39) and (40) scaling with k^4. In Fig. 3, the growth rates for the wavenumber $0.01/H_0$ are plotted for a pressure gradient of $\partial p_g/\partial x = 19.62\,\mathrm{Pa\,m^{-1}}$ as a function of the nondimensional film thickness.

Papaefthymiou et al. (2013) discussed that the weakly nonlinear equations describing systems of arbitrary viscosity ratios should still take a qualitatively similar form as Eqs. (13) and (14). However, expression (40) indicates that for arbitrary viscosities the antisymmetric mode is not necessarily linearly stable in this case. Therefore, for such systems, the mirror symmetry can break down dynamically. A similar feature for the related problem of core-annular flows was obtained numerically by Hu and Patankar (1995).

Appendix 3: Weakly nonlinear analysis

Most linear terms of Eqs. (13) and (14) drop out after substitution of the ansatz for the solution (24). This is a direct consequence of employing a generalized form of the solution used for the linearized equation to describe the weakly nonlinear behavior. For instance, Eq. (13) takes the form

$$\int_{-\infty}^{\infty} \left(\frac{\partial A_+}{\partial \tau}e^{\sigma_+\tau} + \frac{\partial A_-}{\partial \tau}e^{\sigma_-\tau} \right)e^{ikX}\mathrm{d}k$$

$$= -\frac{\partial}{\partial X}\left[\left\{ \int_{-\infty}^{\infty} (A_+e^{\sigma_+\tau} + A_-e^{\sigma_-\tau})e^{ikX}\mathrm{d}k \right\}^2 \right.$$
$$\times \frac{3(1 - H_0)[1 + H_0(3 - 2H_0)]}{(1 - 2H_0)^5}$$
$$+ \left\{ \int_{-\infty}^{\infty} (A_+e^{\sigma_+\tau} + A_-e^{\sigma_-\tau})e^{ikX}\mathrm{d}k \right\}$$
$$\times \left\{ \int_{-\infty}^{\infty} (A_+e^{\sigma_+\tau} - A_-e^{\sigma_-\tau})e^{ik'X}\mathrm{d}k' \right\}$$
$$\times \frac{6H_0(2 + H_0 - 2H_0^2)}{(1 - 2H_0)^5} + \left\{ \int_{-\infty}^{\infty} (A_+e^{\sigma_+\tau} - A_-e^{\sigma_-\tau})e^{ikX}\mathrm{d}k \right\}^2$$
$$\left. \times \frac{3H_0^2(3 + 2H_0)}{(1 - 2H_0)^5} \right]. \tag{41}$$

Since multiplication in the position space transforms to convolution in Fourier space, one finds that

$$\frac{\partial A_+}{\partial \tau}e^{\sigma_+\tau} + \frac{\partial A_-}{\partial \tau}e^{\sigma_-\tau} \tag{42}$$

$$= -\mathrm{i}k\left[\frac{3(1 + 6H_0)}{(1 - 2H_0)^5}(A_+e^{\sigma_+\tau}) \underset{k}{*} (A_+e^{\sigma_+\tau}) \right.$$
$$+ \frac{6(1 + 4H_0)}{(1 - 2H_0)^4}(A_+e^{\sigma_+\tau}) \underset{k}{*} (A_-e^{\sigma_-\tau}) \tag{43}$$

$$\left. + \frac{3(1 + 2H_0)}{(1 - 2H_0)^3}(A_-e^{\sigma_-\tau}) \underset{k}{*} (A_-e^{\sigma_-\tau}) \right]. \tag{44}$$

A similar calculation can be performed for Eq. (14). A straightforward simplification of these two equations leads to the form of Eq. (25).

Appendix 4: Instabilities at vanishing Reynolds number

There are two known instabilities appearing during stratified film flows at zero Reynolds numbers. The first one is the kinetic alpha effect which appears from the resonance-like coupling of the interfaces. According to the results of Kliakhandler and Sivashinsky (1995), this instability is significant for configurations where the intermediate layer is thin. However, Assumption 3 of Sect. 2.2 is only justified if the mean gas velocity is much larger than the velocities at the gas–liquid interfaces. This is not fulfilled for thin gas layers. Thus, the kinetic alpha effect is automatically excluded from the analysis described in this paper.

As it was indicated Kliakhandler and Sivashinsky (1995) as well as by Papaefthymiou et al. (2013), another form of instability could also appear in the system. This instability is induced by the coupling between capillary forces and advective effects, and it has been implied to be a generalization of the Majda–Pego instability (Majda and Pego 1985). It is noted that the validity of this assumption is currently an open question: The Majda–Pego instability has been derived for systems where, instead of a fourth-order spatial derivative, there is only a second-order spatial derivative in the evolution equations for the film thicknesses. Given the limited importance of the instability for the current analysis, herein, only a brief comparison between the corresponding results and those of Papaefthymiou et al. (2013) will be presented. As it was mentioned in the discussion of Eqs. (31) and (32), in symmetric systems, the surface tension always decreases the deformations of the interfaces, and thus, no Majda–Pego instability appears. This agrees with the expectations, as the instability criteria discussed by Canic and Plohr (1995) and assumed by Papaefthymiou et al. (2013) to be valid for quartic dissipative systems cannot be fulfilled. Formally, according to Eqs. (13) and (14), the dissipation matrix of the Majda–Pego instability is defined by

$$\mathbf{D} = \begin{pmatrix} H_0^3/3 & 0 \\ 0 & H_0^3/3 \end{pmatrix}. \tag{45}$$

Since this is a positive multiple of the identity matrix, the system under study is not expected to be unstable in the sense of Majda and Pego. For asymmetric systems, the diagonal elements of **D** are no longer equal; thus, the kinetic instability may appear in such systems. In principle, such a secondary instability could also lead to the observed decoupling of the liquid layers for intermediate values of δ

captured by the numerical simulations of Sect. 4. In the light of the yet unproven applicability of the Majda–Pego instability for the asymmetric systems addressed in this work, the explanation given in the main text appears to be the more profound one.

Appendix 5: Numerical simulations

To support the argument that the antisymmetric mode disappears if the system is initially mirror-symmetric, numerical simulations were performed. The parameters of the simulations are summarized in Sect. 3.2. The results are given in Table 3. The simulated time intervals were set to τ_{max}, the value of which was chosen large enough for $\langle \zeta_+^2 \rangle$ to reach an asymptotic state, i.e., it just oscillates around its asymptotic value. At the last time step, the ratio of $\langle \zeta_+^2 \rangle$ and $\langle \zeta_-^2 \rangle$ is calculated. The results confirm that, after a sufficiently long time, the magnitude of the antisymmetric mode is considerably smaller than that of the symmetric one.

Table 3 Results of the numerical simulations for symmetric configurations

H_0	Re	Ca	ϵ	τ_{max}	$\langle \zeta_+^2 \rangle / \langle \zeta_-^2 \rangle$
0.01	10	0.5	0.1	1200	6.76×10^2
0.02	10	0.5	0.1	800	1.51×10^3
0.05	10	0.5	0.1	400	6.02×10^3
0.1	10	0.5	0.1	40	1.13×10^4
0.2	10	0.5	0.1	20	3.51×10^4
0.3	10	0.5	0.1	2	3.22×10^4
0.1	1	0.5	0.1	500	1.56×10^1
0.1	2	0.5	0.1	80	8.25×10^4
0.1	5	0.5	0.1	80	8.92×10^4
0.1	10	0.5	0.005	20	1.89×10^1
0.1	20	0.5	0.1	80	6.70×10^5
0.1	50	0.5	0.1	60	8.03×10^7
0.1	10	0.125	0.1	20	1.41×10^3
0.1	10	0.25	0.1	20	7.09×10^3
0.1	10	1	0.1	20	1.59×10^4
0.1	10	2	0.1	20	4.43×10^4
0.1	10	5	0.1	40	6.93×10^4
0.1	10	0.5	0.005	40	1.94×10^1
0.1	10	0.5	0.01	40	8.35×10^1
0.1	10	0.5	0.02	40	2.90×10^2
0.1	10	0.5	0.05	40	2.12×10^3
0.1	10	0.5	0.2	40	6.29×10^4
0.1	10	0.5	0.5	40	6.65×10^5

The last column contains the ratio of the magnitudes of the symmetric and the antisymmetric modes at $\tau = \tau_{max}$

Appendix 6: Reduction to single evolution equation

Equations (29) and (30) are reducible to a single evolution equation, even without assuming that $\zeta_- \ll \zeta_+$. To show this, one introduces

$$Z_-(Y) = \int_{-\infty}^{Y} \zeta_- \, dX. \tag{46}$$

After integrating Eq. (30) with respect to X, one finds

$$\zeta_+\big|_X = -\left\{ \frac{(1-2H_0)^4}{6(1+4H_0)Z_-} \left[\frac{1}{\epsilon} \frac{\partial Z_-}{\partial \tau} + \frac{H_0^3}{3} \frac{\partial^4 Z_-}{\partial X^4} \right] \right\}\Bigg|_{X + \frac{12H_0^2}{(1-2H_0)^4}\tau}. \tag{47}$$

Substituting this into (29) and using $\zeta_- = \partial Z_-/\partial X$, one arrives at a single evolution equation for Z_-. The resulting equation is considerably more complicated than the Kuramoto–Sivashinsky equation. Nevertheless, after solving this single equation, one can directly calculate the deformations of the interfaces.

As an equivalent approach, one can also reduce the number of equations by integrating Eq. (29) instead of (30). Subsequently, ζ_- can be computed. This can be applied to arrive at a single evolution equation for the spatial integral of ζ_+. Since, in general, $\zeta_- \ll \zeta_+$, in certain cases, it may be beneficial to use this equation for the simulations to avoid numerical inaccuracies.

References

Anturkar NR, Papanastasiou TC, Wilkes JO (1990) Linear stability analysis of multilayer plane Poiseuille flow. Phys Fluids A Fluid (1989–1993) 2(4):530–541. https://doi.org/10.1063/1.857753

Brennen CE (2005) Fundamentals of multiphase flows. Cambridge University Press, Cambridge

Canic S, Plohr B (1995) Shock wave admissibility for quadratic conservation laws. J Differ Equ 118(2):293–335. https://doi.org/10.1006/jdeq.1995.1075

Chandrasekhar S (2013) Hydrodynamic and hydromagnetic stability. Courier Corporation, Chelmsford

Chang H, Demekhin EA (2002) Complex wave dynamics on thin films. Elsevier, Amsterdam

Charru F, Hinch EJ (2006) Ripple formation on a particle bed sheared by a viscous liquid. Part 1. Steady flow. J Fluid Mech 550:111–121. https://doi.org/10.1017/S002211200500786X

Comsol (2014) COMSOL Multiphysics®. COMSOL Inc, Göttingen

Cross M, Greenside H (2009) Pattern formation and dynamics in nonequilibrium systems. Cambridge University Press, Cambridge

Cvitanovic P, Davidchack RL, Siminos E (2010) On the state space geometry of the Kuramoto–Sivashinsky flow in a periodic domain. SIAM J Appl Dyn Syst 9:1–33. https://doi.org/10.1137/070705623

Drazin PG, Reid WH (2004) Hydrodynamic stability. Cambridge University Press, Cambridge

Eifert A, Paulssen D, Varanakkottu SN, Baier T, Hardt S (2014) Simple fabrication of robust water-repellent surfaces with low contact-angle hysteresis based on impregnation. Adv Mater Interfaces 1(1300):138. https://doi.org/10.1002/admi.201300138

Gondret P, Rabaud M (1997) Shear instability of two-fluid parallel flow in a hele-shaw cell. Phys Fluids 9(11):3267–3274

Grinthal AE, Aizenberg J (2013) Mobile interfaces: liquids as a perfect structural material for multifunctional, antifouling surfaces. Chem Mater 26(1):698–708. https://doi.org/10.1021/cm402364d

Halpern D, Fujioka H, Takayama S, Grotberg JB (2008) Liquid and surfactant delivery into pulmonary airways. Respir Physiol Neurobiol 163(1):222–231

Heil M, Hazel AL, Smith JA (2008) The mechanics of airway closure. Respir Physiol Neurobiol 163(1–3):214–221. https://doi.org/10.1016/j.resp.2008.05.013 **(Respiratory Biomechanics)**

Hewitt G, Hall-Taylor N (1970) Annular two-phase flow. Pergamon, New York. https://doi.org/10.1016/B978-0-08-015797-9.50011-X

Hooper A, Boyd W (1983) Shear-flow instability at the interface between two viscous fluids. J Fluid Mech 128:507–528

Hooper AP, Grimshaw R (1985) Nonlinear instability at the interface between two viscous fluids. Phys Fluids (1958–1988) 28(1):37–45. https://doi.org/10.1063/1.865160

Houshmand F, Peles Y (2013) Convective heat transfer to shear-driven liquid-film flow in a microchannel. Int J Heat Mass Transf 64:42–52

Hu HH, Patankar N (1995) Non-axisymmetric instability of core-annular flow. J Fluid Mech 290:213–224. https://doi.org/10.1017/S0022112095002485

Hyman JM, Nicolaenko B (1986) The Kuramoto–Sivashinsky equation: a bridge between PDE's and dynamical systems. Physica D 18(1–3):113–126. https://doi.org/10.1016/0167-2789(86)90166-1

Johnson M, Kamm RD, Ho LW, Shapiro AH, Pedley TJ (1991) The nonlinear growth of surface-tension-driven instabilities of a thin annular film. J Fluid Mech 233:141–156

Joseph D, Renardy M, Renardy Y (1984) Instability of the flow of two immiscible liquids with different viscosities in a pipe. J Fluid Mech 141:309–317

Joseph DD, Bai R, Chen KP, Renardy YY (1997) Core-annular flows. Annu Rev Fluid Mech 29(1):65–90

Kabov OA, Zaitsev DV, Cheverda VV, Bar-Cohen A (2011) Evaporation and flow dynamics of thin, shear-driven liquid films in microgap channels. Exp Therm Fluid Sci 35(5):825–831

Kandlikar SG (2012) History, advances, and challenges in liquid flow and flow boiling heat transfer in microchannels: a critical review. J Heat Transf 134(3):034001

Kevrekidis IG, Nicolaenko B, Scovel JC (1990) Back in the saddle again: a computer assisted study of the Kuramoto–Sivashinsky equation. SIAM J Appl Math 50(3):760–790

Kliakhandler I, Sivashinsky G (1995) Kinetic alpha effect in viscosity stratified creeping flows. Phys Fluids 7(8):1866–1871. https://doi.org/10.1063/1.868501

Kudryashov N (1990) Exact solutions of the generalized Kuramoto–Sivashinsky equation. Phys Lett A 147(5–6):287–291. https://doi.org/10.1016/0375-9601(90)90449-X

Kuramoto Y, Tsuzuki T (1976) Persistent propagation of concentration waves in dissipative media far from thermal equilibrium. Prog Theor Phys 55(2):356–369. https://doi.org/10.1143/PTP.55.356

Li CH (1969) Instability of three-layer viscous stratified flow. Phys Fluids (1958–1988) 12(12):2473–2481. https://doi.org/10.1063/1.1692383

Lide DR, Haynes WM (eds) (2010) CRC handbook of chemistry and physics, 90th edn. CRC Press, Boca Raton

Majda A, Pego RL (1985) Stable viscosity matrices for systems of conservation laws. J Differ Equ 56(2):229–262. https://doi.org/10.1016/0022-0396(85)90107-X

Nicolis G, Prigogine I (1977) Self-organization in nonequilibrium systems. Wiley, New York

Oron A, Davis SH, Bankoff SG (1997) Long-scale evolution of thin liquid films. Rev Mod Phys 69:931–980. https://doi.org/10.1103/RevModPhys.69.931

Papaefthymiou ES, Papageorgiou DT (2017) Nonlinear stability in three-layer channel flows. J Fluid Mech 829:R2

Papaefthymiou ES, Papageorgiou DT, Pavliotis GA (2013) Nonlinear interfacial dynamics in stratified multilayer channel flows. J Fluid Mech 734:114–143. https://doi.org/10.1017/jfm.2013.443

Reisfeld B, Bankoff SG, Davis SH (1991) The dynamics and stability of thin liquid films during spin coating. I. Films with constant rates of evaporation or absorption. J Appl Phys 70(10):5258–5266. https://doi.org/10.1063/1.350235

Renardy Y (1987) Viscosity and density stratification in vertical Poiseuille flow. Phys Fluids (1958–1988) 30(6):1638–1648. https://doi.org/10.1063/1.866228

Saisorn S, Wongwises S (2008) A review of two-phase gas–liquid adiabatic flow characteristics in micro-channels. Renew Sustain Energy Rev 12(3):824–838. https://doi.org/10.1016/j.rser.2006.10.012

Shlang T, Sivashinsky G, Babchin A, Frenkel A (1985) Irregular wavy flow due to viscous stratification. J Phys Paris 46(6):863–866. https://doi.org/10.1051/jphys:01985004606086300

Sivashinsky GI, Michelson DM (1980) On irregular wavy flow of a liquid film down a vertical plane. Prog Theor Phys 63:2112–2114. https://doi.org/10.1143/PTP.63.2112

Taitel Y, Dukler AE (1976) A model for predicting flow regime transitions in horizontal and near horizontal gas-liquid flow. AIChE J 22(1):47–55. https://doi.org/10.1002/aic.690220105

Talimi V, Muzychka Y, Kocabiyik S (2012) A review on numerical studies of slug flow hydrodynamics and heat transfer in microtubes and microchannels. Int J Multiph Flow 39:88–104

Triplett K, Ghiaasiaan S, Abdel-Khalik S, Sadowski D (1999) Gas–liquid two-phase flow in microchannels part I: two-phase flow patterns. Int J Multiph Flow 25(3):377–394. https://doi.org/10.1016/S0301-9322(98)00054-8

VanHook SJ, Schatz MF, Swift JB, McCormick WD, Swinney HL (1997) Long-wavelength surface-tension-driven Bénard convection: experiment and theory. J Fluid Mech 345:45–78. https://doi.org/10.1017/S0022112097006101

Vécsei M, Dietzel M, Hardt S (2014) Coupled self-organization: thermal interaction between two liquid films undergoing long-wavelength instabilities. Phys Rev E 89(053):018. https://doi.org/10.1103/PhysRevE.89.053018

Weisman J (1983) Two-phase flow patterns. In: Cheremisinoff NP, Gupta R (eds) Handbook of fluids in motion, chap 15. Ann Arbor Science Publishers, Ann Arbor, pp 409–425

Wong TS, Kang SH, Tang SK, Smythe EJ, Hatton BD, Grinthal A, Aizenberg J (2011) Bioinspired self-repairing slippery surfaces with pressure-stable omniphobicity. Nature 477:443–447. https://doi.org/10.1017/S0022112097006101

Yiantsios SG, Higgins BG (1988) Linear stability of plane poiseuille flow of two superposed fluids. Phys Fluids 31(11):3225–3238

Yih CS (1967) Instability due to viscosity stratification. J Fluid Mech 27:337–352. https://doi.org/10.1017/S0022112067000357